



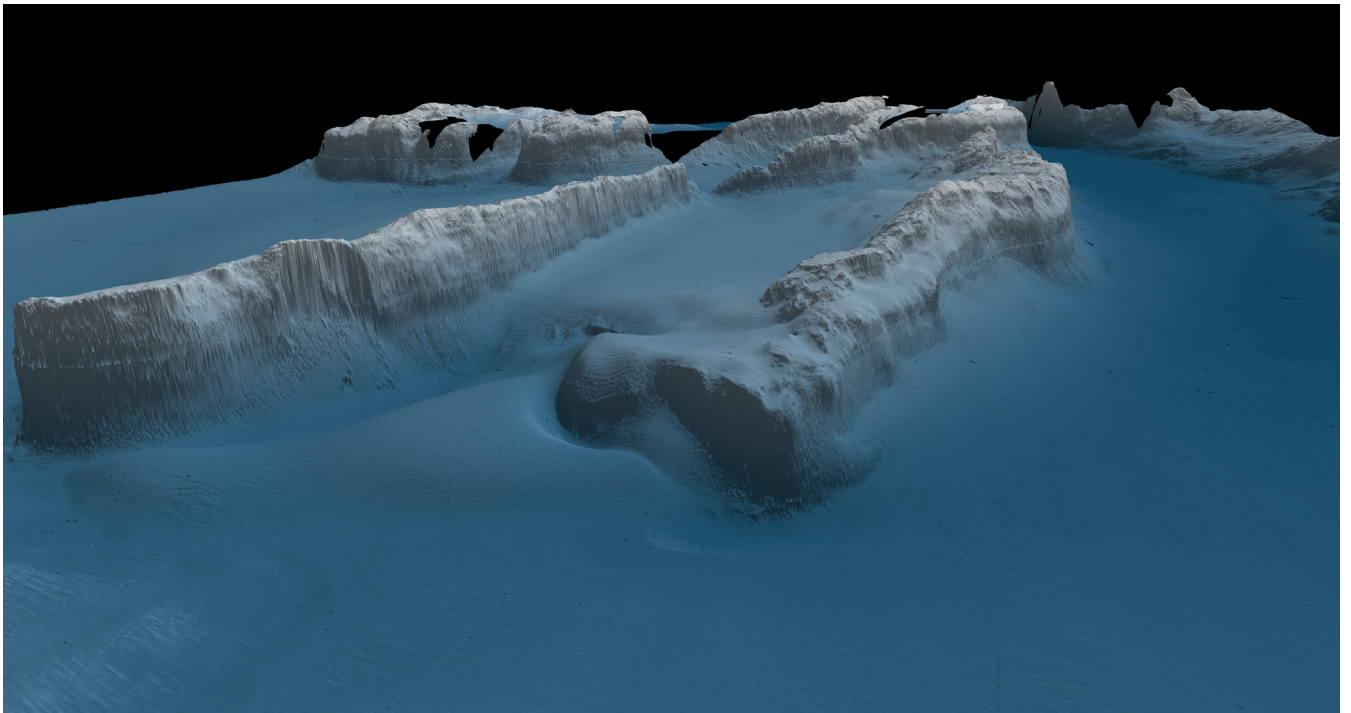
Stockholm  
University

# Master Thesis

Degree Project in  
Marine Geology 60 hp

## Marine Geology and Holocene Paleoceanography of the Southern Quark, Baltic Sea

Anton Wagner



Stockholm 2022

Department of Geological Sciences  
Stockholm University  
SE-106 91 Stockholm

## Abstract

The Understen-Märket trench is located in the Southern Quark and is the only deep-water connection between the Baltic Proper and the Gulf of Bothnia. Bathymetric mapping reveals a number of eroded channels and drift deposits exists on the seafloor, indicating that the area is heavily affected by current activity. Bottom current behavior in the area is not thoroughly understood, but generally in the Baltic Basin, there is southward flowing fresh surface waters compensated by denser northward flowing more saline bottom waters. The dominant direction of flow for bottom waters in the Southern Quark is northward. Northward speeds often exceed the threshold required to erode fine material on the seafloor. Using geophysical data and marine sediment cores, this study shows that current eroded channels and drift deposits in the Understen-Märket trench were initially formed in the late Holocene between 3 – 4 kyr BP, during the transition from the Littorina to the Post Littorina stages of the Baltic Sea. Application of the sortable silt (SS) proxy for current sorting show three distinct regimes that closely match the assigned lithologic units (LU) based on core descriptions. Downcore grain size analysis of three marine sediment cores reveals a gradual boundary to sandy sediments that caps two of the cores recovered from an eroded channel. The third core was recovered from the drift deposit which mostly consists of silt. The progressive coarsening suggests that the current activity has increased during the late Holocene. A simplified model is presented that shows how moderate (20-50 m) shallowing of the sill, which has occurred in response to isostatic rebound between 8 and 4 kyr BP, could have generated the higher current speeds seen today. However, this should be explored using more advanced paleo-circulation models.

**Keywords:** Bottom currents, sortable silt, radiocarbon dating, Baltic Sea stages, estuarine circulation, marine sediment cores, marine geophysical mapping.

# Contents

Abstract .....	1
1. Introduction.....	4
2. Background.....	6
2.1. Baltic Sea Since the Last Deglaciation .....	6
2.2. Southern Quark Oceanography.....	8
3. Method.....	9
3.1. Geophysical Data.....	9
3.1.1. Multibeam Echo-sounder (MBES) .....	9
3.1.2. Sub-bottom Profiler.....	10
3.2. Geophysical Data Processing.....	10
3.2.1. MBES Data .....	10
3.2.2. Sediment Thickness and Surface Interpolation.....	11
3.3. Sediment Coring .....	12
3.3.1. Visual Core Description .....	12
3.4. Loss on Ignition.....	12
3.5. Grain Size Measurements.....	13
3.5.1. Sortable Silt Processing .....	13
3.6. Radiocarbon Dating & TOC.....	14
4. Results .....	14
4.1. Geophysical Results.....	14
4.2. Sub-Bottom Profiles .....	17
4.2.1. Sediment Thickness Compilation .....	19
4.2.2. Acoustic Appearance at the Coring Sites .....	20
4.3. LOI.....	21
4.4. Radiocarbon Dating and TOC .....	23
4.5. Grain Size.....	25
4.5.1. Surface Sediment.....	25
4.5.2. Downcore Grain Size .....	25
4.5.3. SS% and SS correlation .....	26
5. Discussion .....	28
5.1. Current Controlled Sedimentation.....	28
5.2. Sediment Age & Stratigraphy .....	29
5.3. Environmental Conditions at the Onset of the Post-Littorina Sea.....	31
5.3.1. Paleocurrent Strength Calculations Based on Shallowing from Isostatic Rebound .....	32
6. Conclusion .....	33

Acknowledgements .....	34
References.....	34
Appendix A .....	39
Appendix B .....	40

# 1. Introduction

Circulation in the Baltic Sea has undergone many changes during the Holocene. Variations between fresh- and brackish water affected the degree of stratification in the water column and impacted the oxygen conditions of bottom waters (Jilbert et al., 2015; Jilbert and Slomp, 2013). Due to large freshwater input in the northern part of the Baltic, there is currently a permanent sea level tilt that drives less dense fresh- to brackish surface water south towards the Danish strait. This outflow of less saline surface waters is compensated by a corresponding inflow of dense saline water bottom water (Szymczycha et al., 2019). The Danish strait and Öresund are currently the Baltics only connection to the ocean where saline water enters the Baltic after passing over shallow sills, roughly 10-20 m deep (Håkanson and Bryhn, 2008; Widerlund and Andersson, 2011). During the deglacial and early to middle part of the Holocene (around 10.7 – 11.7 and 6 – 8 kyr BP), this connection was much deeper which occasionally led to large influxes of sea water, bringing oxygen and nutrients that enhanced primary production. This resulted in higher organic carbon content (OC) burial in the seafloor that under hypoxic conditions is reflected in the sediment OC content and by black sulfide bands/mottling in the laminations. (Andrén and Sohlenius, 1995; Wastegård et al., 1995). This deeper connection and stronger inflow around 6 – 8 kyr BP allowed the saline water to travel to the northern basins of the Bothnian Sea and Bothnian Bay. Since then, isostatic rebound has caused shallowing of the entire Baltic but with the emergence of several sills that have restricted the deep-water exchange (Raateoja, 2013).

The main deep-water connection that links the Baltic Proper to the Bothnian Sea (Hietala et al., 2007), known as the Understen-Märket trench, is located in the Southern Quark in the northern Åland Sea (Figure 1). Sedimentary formations, such as contourite drifts and erosional channels found in the region indicate a strong control of bottom currents on sedimentary processes (Jakobsson et al., 2019; Moros et al., 2020). Several sediment cores recovered from the region are capped by a cm- to dm- thick coarse-grained unit (Holmlund et al., in press). This, along with the seafloor formations imply that the sediment has undergone resuspension where to a first order, the force required for eroding and transporting sediment is determined by the current strength and the size of the particle (Hjulström, 1935; Hsu, 2016). Grainsize distributions in sediments can be used to determine the degree of current sorting and semi-quantitatively reconstruct past current (Culp et al., 2020; McCave et al., 2017, 1995). Sortable silt (SS), defined as the silt size class that lies between 10-63  $\mu\text{m}$ , is the most sensitive size fraction for current sorting as larger grains are too heavy, and smaller particles tend to be cohesive, or flocculate in the water column to form larger particles. This size fraction is referred to as Sortable Silts (SS) and grains in this size range exhibit a non-cohesive behavior. This means that the grains largely respond as single particles to hydrodynamic forces of deposition and erosion. Grains  $>63 \mu\text{m}$  is classified as sand and demand higher current velocities to be sorted which may erode or re-suspend finer material (McCave et al., 1995). Laboratory studies have shown that current velocities between 5-25  $\text{cm s}^{-1}$ , common for deep sea environments, have a close to linear correlation to the mean SS size ( $\overline{SS}$ ). As a result,  $\overline{SS}$  is commonly used as a proxy for paleocurrent flow speeds (Culp et al., 2020; McCave et al., 2017).

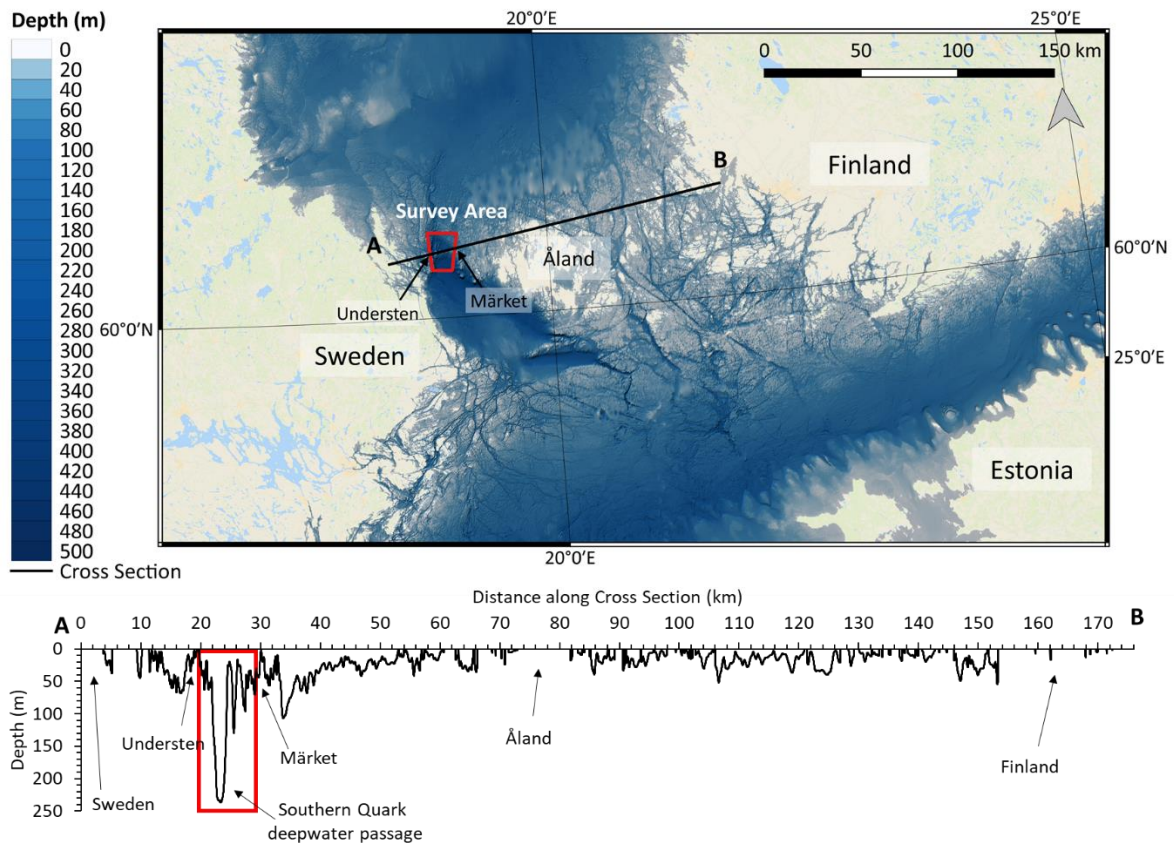


**Figure 1.** Bathymetric map of the central Baltic Sea with the survey area marked in red and cross section shown as a black line between A and B. Bathymetry map courtesy of EMODnet (EMODnet Bathymetry Consortium, 2020). Cross section created using the qProf plugin in QGIS with EMODnet bathymetry as reference layer with 0 as the sea level and each datapoint 20 m apart.

In the summer of 2017, expedition EL17-IGV04 with Stockholm University Research Vessel (RV) *Electra* acquired geophysical data and six sediment cores from the Southern Quark. The field work formed a part of a project supported by the Swedish Radiation Safety Authority aimed to investigate the deglacial dynamics of the Scandinavian Ice Sheet and evidence of mass-wasting in the area. Initial compilation of coring and geophysical data (bathymetry/sub-bottom) revealed a number of sedimentary features and bedforms that indicated current activity in the region. Bathymetric data showed several channels and drift deposits which also suggest large scale current scouring of the seabed in this region. Multi-Sensor Core Logger (MSCL) data showed that several cores were capped by a relatively thin (cm- to decimeter thick unit with higher bulk density, magnetic susceptibility, and P-wave velocity. This suggest ether a coarse lag deposit on the seafloor (formed by ongoing erosion/non-deposition), or the progressive development of current activity which led to an upcore coarsening of grainsize (Holmlund et al., in press). The purpose of this project is to document the influence that bottom current activity has had on the Southern Quark throughout the Holocene and investigate how or when modern circulation developed.

The two hypotheses are 1) The modern northward bottom water flow in the Southern Quark intensified in the late Holocene, the timing of this can be determined through analysis of marine sediment cores and tied to wider environmental change in the Baltic, and 2) The development of the erosional channels and drift deposits in the Southern Quark were synchronous. Drift deposits started to form when current scouring started to erode the channels along the flanks of bathymetric highs. Therefore, the deepest sediments sampled from the drift deposit should be younger than the lithologic transition marking the onset of scouring in sediments sampled from the channels.

## 2. Background

### 2.1. Baltic Sea Since the Last Deglaciation

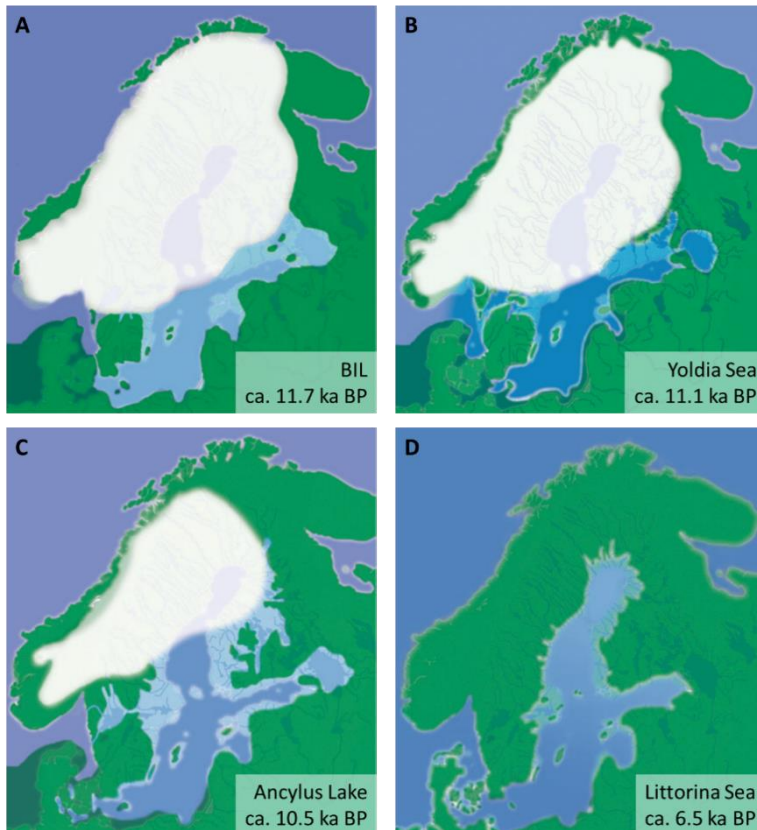


**Figure 2.** Paleogeographic map of the different stages of the Baltic history throughout the Holocene since the last deglaciation. A) BIL just before the final drainage and maximum extension. B) Yoldia Sea at the end of the brackish stage. C) Ancyclus Lake at the maximum transgression. D) Littorina Sea during its most saline phase (figure modified from Andrén et al., 2011).

margin halted and briefly began advancing southward (Andrén, 2012; Andrén et al., 2011). At the end of the Younger dryas cold phase the ice sheet continued to retreat northward. Once the ice front reached the slope of Mt. Billingen, Västergötland, a passage between the ice and the mountain was exposed and allowed rapid drainage of the BIL (Mörner, 1995). This resulted in a water level drop of 25 m in one or two years, which corresponds to roughly 7,800 km<sup>3</sup> of fresh water (Jakobsson et al., 2007). The total sediment thickness deposited during the BIL ranges from several meters to often tens of meters and is characterized by varved glacial clays. Generally thicker varves are observed closer to the ice margin. These become tinner and grade into greyish clayey/silt with occasional brownish layers and lenses further from the ice margin (Winterhalter, 1992).

The drainage of the BIL signified the end of the Younger Dryas and beginning of the Yoldia Sea, which also coincides with the start of the Holocene epoch at ~11.7 kyr BP (Figure 2B, Andrén et al., 2011; Walker et al., 2009). Increasing temperatures of up to 12°C led to continued melting of the ice and more meltwater compared to the BIL stage. The amount of outflowing water hindered saline water from entering the basin despite being connected to the ocean (Andrén, 2012). Saltwater first began to enter the Yoldia Sea approximately 300 years after drainage of the BIL. Reasons for this have been attributed to widening of the straits between the ice margins and land topography as well as a short cold period which reduced the meltwater outflow (Andrén, 2012). The inflow of saline water also brought nutrients that increased production of zoo- and phytoplankton. This is reflected in an overall increase in the organic carbon content of Yoldia Sea sediments from the Baltic. Fossilized mollusks, shells and other

The development of the Baltic Sea began during the last deglaciation with the formation of the Baltic Ice Lake (BIL), ca. 16 kyr BP (Figure 2A, Andrén et al., 2011). Rapid melting of the Scandinavian ice sheet led to large volumes of water that drained into the North Sea through the Öresund area. Due to the fast accumulation of meltwater and continuous outflow, erosion of the Öresund strait took approximately 500 years until it reached the bedrock 7 m below the water level. Glaciostatic rebound caused the threshold of this outlet to rise above local sea level, blocking outflow and leading to the development of the large Baltic ice lake (Andrén, 2012; Björck, 1995). This warming period resulted in a first drainage of the BIL around 13 kyr BP (Swärd et al., 2015), but was interrupted roughly 12.9 kyr BP by a 1300 year cold period known as the Younger Dryas (Hartz, 1912). As a result, the retreat of the ice

microscopic diatoms have also been found in the sediments from this stage (Andrén and Sohlenius, 1995; Björck, 1995; Wastegård et al., 1995). Isostatic rebound during this time caused the straits connected to the ocean to become shallower and narrower which decreased the inflow of saltwater. Hence, the shoaling of sills and reduced saltwater inflow marked the end of the Yoldia Sea (Andrén, 2012; Andrén et al., 2011). Sediments from the Yoldia Sea stage have been difficult to define since it does not display a clear lithologic boundary that marks an end to the marine influence. However, a characteristic feature of Yoldia Sea sediments are black sulfide stains/bands. One possibility is that these developed due to the brief inflow of saltwater that then created a strong halocline, reduced mixing and allowed anoxic conditions to develop in bottom waters (Andrén, 2012; Winterhalter, 1992).

The next stage in the Baltic Sea history was the freshwater Ancylus Lake that began approximately 10.7 kyr BP (Figure 2C). This is the least understood stage in the Baltics history. There have been many discussions of how it formed, progressed and ended (Andrén, 2012; Björck, 1995; Jensen et al., 1999). The current consensus is that the Ancylus Lake was a damned-up due to isostatic uplift, with the water level in the Baltic basin to be ~10 m above the North Sea's current sea level (Björck et al., 2008). Due to higher uplift rate in northern Sweden compared to southern Sweden, the water level rose rapidly in the south which led to one or more drainage outlets occurring in this region (Andrén, 2012). The outflowing freshwater to the North Sea was rapid and lowered the shoreline by ~5 m around 10 kyr BP. Short and sporadic pulses of saline water inflow occurred and resulted in periodic brackish conditions that have been identified in sediments from the Gotland and Bornholm basins as early as ~9.8 kyr BP. This was the first sign of a new Baltic stage, but it would take 1000-1500 years for the saline water to reach the northern parts of the Baltic (Andrén, 2012; Björck et al., 2008). Due to the relative absence of saline water during the Ancylus Lake stage, stratification of the water column was limited, and seasonal mixing occurred. The sediments from this stage are often described as transitional clays consisting of homogenous clays and black sulfide mottled clays (Wastegård et al., 1995; Winterhalter, 1992; Winterhalter et al., 1981).

Inflow of new saline oceanwater in the southern part of the Baltic basin once again resulted in the development of a strongly stratified water column, with brackish water conditions and estuarine circulation (Virtasalo et al., 2014). This is referred to as the Littorina Sea stage (Figure 2D). The increase in overall salinity caused flocculation of suspended clay particles that deposited on the sea floor. Light penetration into the water column increased as a result of this, and coupled with the influx of nutrients, led to higher primary production (Sohlenius and Westman, 1998). Increased organic carbon content and a spongy texture to the sediments are characteristic features of Littorina Sea sediments (Winterhalter, 1992). Since the Scandinavian Ice Sheet no longer covered any part of the Baltic basin, isostatic rebound still caused land uplift. Warmer atmospheric temperatures lead however to global sea-level rise, which in the southern Baltic basin exceeded the land uplift rate and, at approximately 6.5 kyr BP, caused a 5 m higher relative sea level than today (Andrén, 2012; Berglund et al., 2005). It was at this point when the salinity in the basin is believed to be at its highest, but how saline is still debated. Oxygen isotopes from fossil shells found in the Gulf of Finland do however indicate a ~4% higher salinity than today (Donner et al., 1999). Both the water level and salinity decreased after this peak. Possible reasons for the decline in salinity and the long-term trend towards present conditions could be reduced inflow of ocean water from the North Sea, as well as lower summer temperatures and increased precipitation, and river runoff in the Baltic catchment area (Björck et al., 2008; Gustafsson and Westman, 2002). The Littorina sea stage ended when the Baltic basin attained its present conditions about 3 kyr BP, and the current stage is sometime referred to as the Limnea Sea, or Post Littorina Sea (Virtasalo et al., 2014; Winterhalter et al., 1981). The difference between Littorina and Post Littorina sediment is difficult to pinpoint, but the Littorina sediment is generally slightly more bioturbated and often categorized as gyttja or gyttja clay, while Post Littorina sediments is often described as homogenous muds. Due to the poor compaction, the texture of both stages is quite loose and spongy and differ acoustically from more compact underlying sediments. Both stages also contain varying to high amounts of organic matter (OM), which due to the hypoxic conditions usually is dark/black in color (Winterhalter, 1992).

## 2.2. Southern Quark Oceanography

Semi-enclosed bodies of water that are connected to the ocean attain a certain kind of circulation referred to as estuarine circulation. The definition, proposed by Pritchard (1967), of an estuary is that it is where saline ocean water is measurably diluted by freshwater draining from land. Four typical types of estuary circulation are known to exist, (1) Salt wedge, which is when a nearly stationary dense saline body of oceanwater rest on the seafloor and fresh river water flows on top of it towards the mouth of the estuary. The halocline is often sharp and creates friction between the water masses and can form small waves of saline water when the shear velocity is high enough that can break and mix with the fresh surface water. (2) Partially mixed circulation is a more efficient way of mixing the saline oceanwater with the fresh land runoff water than salt wedge mixing. This is created by a faster inflow of oceanwater that creates turbulence and more effective mixing the water layers. The halocline in a partially mixed circulation system has a more gradual gradient both within the water column and along the estuary reach. (3) Well-mixed estuarine circulation is produced by turbulent mixing throughout the water column due to the waterflow across the seafloor in areas prone to macrolides ( $6\text{m} > \text{tides} > 4\text{m}$ ) or hypertides ( $\text{tides} > 6\text{m}$ ) (Davies, 1964; Dyer, 2001; Kirk Cochran, 2014). (4) Fjord-type circulation has also been described as a separate type of estuarine circulation. A shallow sill in the mouth of a fjord restricts high velocity inflow of saline bottom water that limits vertical mixing leading to strong stratification with a pronounced halocline (Kirk Cochran, 2014).

Oceanic exchange between the Baltic proper and Bothnian Sea is impeded by a narrow (30 km) strait between Sweden and Finland known as the Åland Sea. Several sills in the area make out the main barrier which hinders the saline deep-water originating from Kattegat to reach the Bothnian Sea and later the Bothnian Bay. Åland Sea is restricted by two sills that separates it from the Baltic Proper in the south (40 m deep). The other separates it from the Bothnian Sea further north between Understen and Märket (10-30 m deep). The latter sill is however cut by two deep canyons in the east and central part of the region (200m and 100 deep respectively) (Marmefelt and Omstedt, 1993). This reduces the ventilation of the deep-water in the northern basins and results in a mean age of the water mass below the halocline depth (~35-40m) to be roughly 24 and 40 years in the Bothnian Sea and Bothnian Bay respectively (Meier, 2007).

The direction of flow within the water column is highly variable in short term observations (days) (Ehlin et al., 1977). While on longer timescales (months to years) an average southward surface current and northward bottom current have been observed (Figure 3) (Palosuo, 1964; SMHI, 2021). Measurements

made in 1976 supports this by reporting a weak northward current below 60 m and a stronger southward surface current (Ambjoern and Gidhagen, 1979). A recent study using a model based on the Nucleus for European Modeling of the Ocean (NEMO), of water transport in the Åland Sea agrees with these findings (Gurvan et al., 2022; Westerlund et al., 2022). The cause for this current behavior has been attributed to that the Baltic Sea and certain subbasins within it resembles estuary circulation systems. On longer timescales, the amount of salt transfer

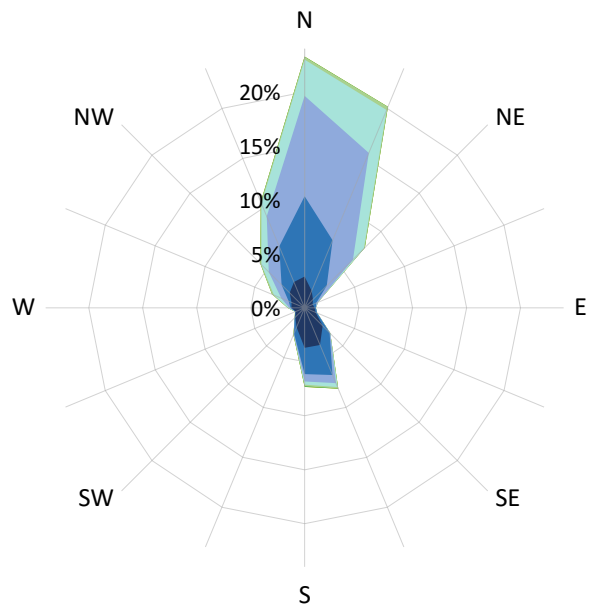
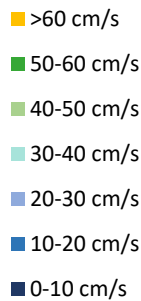


**Figure 3.** Rose-plot showing current direction and speed measured just east of Understen at a water depth of 220 m during the period Dec 2020 to Dec 2021. The plot shows some fluctuation in current direction but is predominately northward most of the year (data from SMHI, 2021).

flowing in and out of a basin, Bothnian Sea in this case, should be equal. Weak dense saline inflowing bottom currents should be compensated by stronger less saline outflowing surface currents based on observations made by Knudsen (1900), and his theory on estuary systems.

### 3. Method

#### 3.1. Geophysical Data

To acquire a detailed view of the seafloor and sub-surface sediment structures, two types of geophysical instruments were used, multibeam echo-sounder and sub-bottom profiler. During the EL17-IGV04 expedition roughly 80 km<sup>2</sup> of bathymetry data and 25 Sub-bottom profiles were collected using the research vessel RV *Electra af Askö*.

##### 3.1.1. Multibeam Echo-sounder (MBES)

Bathymetry was collected using a Kongsberg EM2040 0.4°×0.7°, 200-400 kHz multibeam echo-sounder that is hull-mounted on the research vessel RV *Electra af Askö*. The 0.4° transmit transducer array is mounted along ship and is 727×142 mm (L×W), while the 0.7° receive transducer array is mounted across and is 407×142 mm (L×W). The EM2040 can log acoustic data of the water column and is capable of mapping in water depths of up to 600 m. The swaths are however dependent on the selected frequency (wider swaths with lower frequency), bottom type, and water properties. It is operated by the Kongsberg's Seafloor Operation System (SIS) version 4.3.2 (build 31, DBVersion 30.0).

Most of the area was mapped at a frequency of 300 kHz, aiming at 100% overlapping swaths between the survey lines with a cruising speed of 5-6 knots. A higher frequency of 400 kHz was briefly utilized in part of the area when passing over the shipwreck *August Thyssen*. Due to the significant depth variation, the survey lines could not be kept straight to maintain a 100% overlap. Midwater and sub-bottom profiles were collected separately from the multibeam bathymetry in order to keep the highest ping rate possible.

### 3.1.2. Sub-bottom Profiler

Aft of the multibeam, RV *Electra* is equipped with a Kongsberg Topas PS40, 24ch, parametric sub-bottom profiler. It can operate either as a continuous wave or chirp pulses to create sub-bottom profiles (SBP). The transducer produces two kinds of acoustic pulses, a primary and a secondary, at 35-45 kHz and 1-10 kHz respectively. Where the secondary acoustic pulse is produced by non-linear interaction between two primary pulses. The hydrophone which receives the reflected acoustic pulse is 340×180 mm (L×W), and the transmit transducer is 830×540 mm (L×W). For this cruise, a chirp pulse with a bandwidth (B) between 2-10 kHz was used, which results in an approximate vertical resolution ( $R_v$ ) of ~0.1 m assuming a sediment sound velocity ( $v$ ) of 1500 m/s (equation 1).

$$R_v = \frac{v}{B*2} \quad \text{Equation 1}$$

## 3.2. Geophysical Data Processing

### 3.2.1. MBES Data

Processing of MBES data involved several steps. To remove artifacts and correct for possible imperfections in the data, the multibeam processing software Qimera was used (version 2.4.2 from QPS). Due to the large depth variations in the survey area, the projected cell size was divided into three sections with different resolutions to retain as much detail as possible. To estimate the appropriate cell size for the 3 sections, the footprint (F) for the multibeam was calculated using equation 2 as a guideline. Trial and error were then used to pick appropriate cell sizes, since the calculated result was not necessarily the most applicable. The shallowest section was displayed from the water surface to a depth of 120 m and was projected at a cell size of 1.75 m. The next section was from 40 m to 200 m where a 2.75 m cell size was chosen. The final section was displayed from 120 m to 250 m with a 4 m cell size. The 80 m overlap of section 2 and 3 was chosen to cover any potential gap which may have been caused by applying different cell sizes to each section in the map compiling software QGIS.

$$F = 2D * \tan\left(\frac{\alpha}{2}\right) \quad \text{Equation 2}$$

Where D is the water depth from the transmitter to the seafloor and  $\alpha$  is the transducer array angle.

The three sections were combined into a dynamic surface using the Combined Uncertainty and Bathymetry Estimator (CUBE) algorithm which statistically processes the data to remove errors gathered from the multibeam echosounder (MBES) (Calder and Mayer, 2003). Despite the coarse resolution of 4 m in the deepest parts of section 3, there were still gaps in the data. These holes were filled by interpolating the dynamic surface by using the average values from the 5 nearest neighbors. When a smooth dynamic surface was created, some artifacts were still apparent, most notably “wobbly outer beams” (Figure 4A). Such artifacts may be the result of non-accounted for offsets between the motion sensor, the navigation systems GPS sensor and transducer, or time syncing problems between these. It could also be accentuated by poor sound speed control in the water column, which was the reason in this case. TU Delf Sound Speed Inversion in Qimera corrects for problems in the bathymetric data caused by sound speed and allows for automated refraction error correction. This, along with a patch test which accounted for misalignments in roll offsets, 0.08° in this case, caused by the vessel were carried out to minimize these artifacts (Figure 4B).

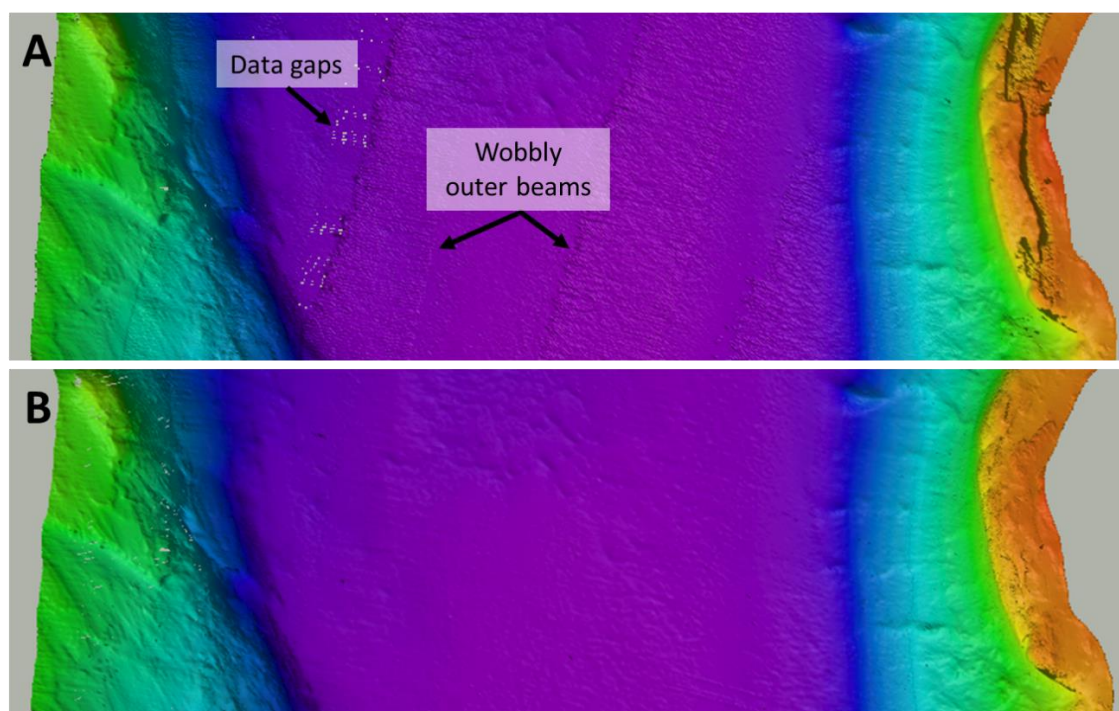


**Figure 4.** Same areas of the sea floor in A & B where the purple represent the deepest parts plotted with a cell size of 4 m. A) Surface is partly cleaned but with no surface interpolation, sound speed inversion nor patch tests completed. B) Cleaned data along with surface interpolation, sound speed inversion and patch test preformed.

#### 3.2.1.1. Backscatter & ARA Analysis

MBES systems acquire depth information by measuring the travel time of a sound pulse from the transmitter to the seafloor and back to the receiver. This information is used to create bathymetric maps (Jakobsson et al., 2016). By measuring the intensity of the reflected sound pulse, properties of the surface sediment can be estimated. Such properties are the grainsize, seafloor roughness and compaction along with any biological substrate if present (Le Bas and Huvenne, 2009). Regular uncalibrated backscatter does however neglect the incidence angle of the sound pulse to the seafloor, as well as other critical parameters such as source level. This implies a large variation in backscatter on the multibeam acquisition. Angular range analysis (ARA) has therefore been developed to account for specifically for the incidence angle and pulse range. ARA can thus be used for remote estimation of the seafloor properties. The difference with respect to regular backscatter is that ARA combines between 20 to 30 sonar pings to approximate the dimension of the swath width along the path direction, whereas backscatter applies a radiometric correction to each cell from one or more lines (Fonseca and Mayer, 2007). This results in a larger file containing more information from the backscatter mosaic since each sonar ping is plotted in a cell. The ARA image is a smaller file since it consists of patches created from up to 30 pings which in turn leads to a coarser resolution image but can generally tell you more about the seafloor properties, in particular parameters influencing roughness such as grain size.. Verification and comparison of the backscatter analyses is important to give an accurate representation of the grain size in the area. This is done by collecting samples from the seafloor surface of all six cores and measuring the grain sizes which is further explained in section 0. Since the ARA analysis output a particular response at the place of coring and the measured grain size is known, the output response and grain size can be coupled and thus be used to estimate grain sizes in areas with different ARA output responses.

#### 3.2.2. Sediment Thickness and Surface Interpolation

A total of 25 sub-bottom profiles were collected during the cruise around the Southern Quark. The horizontal extent of the acoustic basement was defined in all profiles with an assumed sound velocity of 1500 m/s using the SonarWiz v.7 software (Chesapeake Technology). Using the natural neighbor

algorithm for interpolation between the sub-bottom profiles, a coherent surface is generated based on a similar method as Thiessen polygons but creates a much smoother surface as it accounts for the weights of proportionate areas to a query point (Sibson, 1981). This surface was then imported into QGIS for further processing and visualization.

### 3.3. Sediment Coring

To recover sediment from the survey area, two types of corers were used, a piston- and gravity corer. The difference being that a gravity corer slowly penetrates the sediment under its own weight, while a piston corer is released by a trigger weight and generally free-falls 1-3 m before impacting and penetrating the seafloor. During the cruise, the corer was equipped with an 859 mm long core head loaded with 476 kg. PVC liners of 6 m in length with an inner/outer diameter of 110/98.5 mm were used. The trigger weight used with the piston core consisted of a 1 m long transparent polycarbonate gravity corer with an inner/outer diameter of 88/80 mm. Retrieved cores were cut into 1.5 m sections and stored in a specifically designed refrigerator which was placed on the aft deck. A total of six cores were collected during the cruise. Three were analyzed in this project (Table 1).

*Table 1. Metadata of the 6 collected cores. Cores 01-PC1, 02-GC1 and 03-PC1 was investigated as emphasized by the dotted line.*

Core	Date (ddmmyy)	Lat	Lon	Water Depth (m)	Core Length (m)	Number of Sections	Short Name
EL17-IGV04-01-PC1	150817	60° 21.1758	18° 58.9081	180	4.77	4	01-PC1
EL17-IGV04-02-GC1	150817	60° 20.8447	18° 57.046	202	4.06	3	02-GC1
EL17-IGV04-03-PC1	170817	60° 21.3757	18° 57.6794	207	4.33	3	03-PC1
EL17-IGV04-04-PC1	170817	60° 19.9996	18° 57.6722	146	5.04	4	04-PC1
EL17-IGV04-05-GC1	170817	60° 19.3446	18° 57.6711	149	5.7	4	05-GC1
EL17-IGV04-06-GC1	170817	60° 20.784	18° 57.0406	197	5.36	4	06-GC1

#### 3.3.1. Visual Core Description

All cores were split, imaged, and described in the SLAM-lab at Stockholm University during the spring of 2021. An exception was made for core 04-PC1 as prior analyses were made on this core before this project began. Color, texture, smell, and grain size of the sediment were recorded in the descriptions and distinctive changes were marked. The core descriptions were later compared to identifying similar lithologic units (LU) that could be matched to the MSCL core logging data. The descriptions of all six cores can be found in the cruise report (Holmlund et al., in press).

#### 3.4. Loss on Ignition

Loss on ignition (LOI) was analyzed to obtain preliminary information on the organic content of the sediment. 12 samples were taken from the three cores. Samples between 5-20 g were dried and weighed. All samples were then put in an oven at 105°C overnight (or >4h) to dry. Once dry, the samples were weighed and then placed in a furnace. Temperature in the furnace was gradually raised to 550°C over two hours and then maintained at that level for eight hours. After eight hours, the temperature was reduced to 105°C where it remained until the next day when they were extracted from the furnace and weighed again. The organic carbon content is determined by dividing burned mass ( $M_b$ ) with the dry mass ( $M_d$ ) of the samples (Equation 3) (Ben-Dor and Banin, 1989; Heiri et al., 2001). Since this method's main purpose was to give a rough estimate of the OC prior to grain size measurements, no adjustment factor was used in the calculation.

$$LOI (\%) = \left(1 - \frac{M_b}{M_d}\right) * 100 \quad \text{Equation 3}$$

### 3.5. Grain Size Measurements

Measurement of the grain size was performed with the particle size analyzer (PSA) Mastersizer 3000 from Malvern Panalytical. This PSA uses laser diffraction to estimate the size fraction of sediment suspended in deionized water. Wet sediment was added to the PSA until an obscuration of 5-15% was reached. 3 ml of sodium hexametaphosphate ( $\text{Na}_6[(\text{PO}_3)_6]$ ) was added three minutes before the test began to ensure that all particles were dispersed. Five replicate measurements were performed on each subsample and two separate subsamples were run on each sample to mitigate any potential errors. The result used was the mean of these 10 measurements.

Determination of grain size require preparation of the sediment and removal of components other than terrigenous material (McCave et al., 1995). Results from the LOI measurements, indicating relatively large amounts of OC, motivated the removal of the OM prior to measuring the grain size. Untreated samples were mixed with deionized water to a total volume of 5-15 ml. Hydrogen peroxide ( $\text{H}_2\text{O}_2$ ) with a concentration of 30% was added to the solution in intervals until there was no visible emanation of  $\text{CO}_2$  bubbles. This process took several days (Table 2). Once the solution had stabilized, the sample tubes were placed in a centrifuge (model Mega Star 1.6 from VWR) at 4200 rounds per minute (rpm) for ten minutes. The supernatant was carefully siphoned off and deionized water was added to the samples and shaken before being placed in the centrifuge again. This process was repeated three times to ensure the sediment was free from  $\text{H}_2\text{O}_2$ . Once clean, deionized water was added to each sample until the total volume of sediment and water was 15 ml. With the use of a stirrer and ultrasonic bath when needed, the sediment was stirred vigorously to remove any lumps or cohesion of grains. A subsample was extracted with a pipette as it was being mixed, and this subsample was added to the PSA.

**Table 2.** Volume of  $\text{H}_2\text{O}_2$  added each day of the sediment sample treatment. Surface samples were extracted 0-1 cm.b.s.f. from all 6 cores that were collected on the cruise. 01-PC1, 02-GC1 and 03-PC1 is the cores that were investigated in more detail. Complimentary samples refer to a total of 12 additional samples that were extracted to increase the sample resolution in the top of 02-GC1 and 03-PC1.

Surface samples		01-PC1		02-GC1		03-PC1		Complimentary samples	
Day	Volume $\text{H}_2\text{O}_2$ (ml)	Day	Volume $\text{H}_2\text{O}_2$ (ml)	Day	Volume $\text{H}_2\text{O}_2$ (ml)	Day	Volume $\text{H}_2\text{O}_2$ (ml)	Day	Volume $\text{H}_2\text{O}_2$ (ml)
1	8	1	10	1	10	1	10	1	5
2	6	8	10	4	10	2	10	2	5
3	6	12	5	6	DONE	3	5	3	10
4	5	15	5			5	5	5	5
7	DONE	16	DONE			9	DONE	8	DONE

#### 3.5.1. Sortable Silt Processing

The PSA measure grain sizes between 0.01-3500  $\mu\text{m}$ . These are categorized into 103 percentages classes (or bins). The data is exported to Excel for further processing. The sortable silt range is between 10-63  $\mu\text{m}$ , however, neither 10 or 63  $\mu\text{m}$  are standard divisions of the bins and therefore had to be interpolated. The interpolation was executed according to the method outlined by McCave and Andrews (2019). The sortable silt fraction of the fines was then calculated ( $\text{SS}\% = \text{sum fraction between 10-63 } \mu\text{m} \text{ divided by the total silt and clay fraction, } <63 \mu\text{m}$ ). The correlation between the  $\text{SS}\%$  and the mean SS size ( $\overline{\text{SS}}$ ) is an indicator for how well current sorted the sediments are.  $\overline{\text{SS}}$  was calculated by applying the “sumproduct” command in Excel on the percentage bins multiplied by the natural logarithm of the size-bins geometric mid-point (Blott and Pye, 2001; McCave and Andrews, 2019), and dividing that with the amount of sediment in the 10-63  $\mu\text{m}$  range.  $\overline{\text{SS}}$  was then plotted against  $\text{SS}\%$  to acquire the correlation

coefficient, which according to McCave and Andrews, (2019) needs to be  $>0.5$  to confidently say that sediments have been current sorted.

### 3.6. Radiocarbon Dating & TOC

Twelve samples of approximately 3-5 g wet bulk sediment were freeze dried and submitted to ETH, Zürich for bulk sediment radiocarbon dating. The samples were taken with the aim to constrain the age for onset of the coarse-grained uppermost unit in 02-GC1 and 03-PC1, and to get a downcore sequence of ages from the drift deposit in 01-PC1 (Figure 5). The hypothesis is that the drift deposit started to form when the current scouring at site 02-GC1 and 03-PC1 began. The oldest dated age from 01-PC1 should therefore be younger than the onset of scouring at the other two sites.

Calibration of the raw radiocarbon ages is needed to account for changes in the atmospheric concentration of  $^{14}\text{C}$  over time. This was performed on all 12 samples on the calib.org website, version 8.20 using the IntCal20 calibration curve from Reimer et al., (2020). No reservoir correction was used as the amount of OC of marine origin is not known.

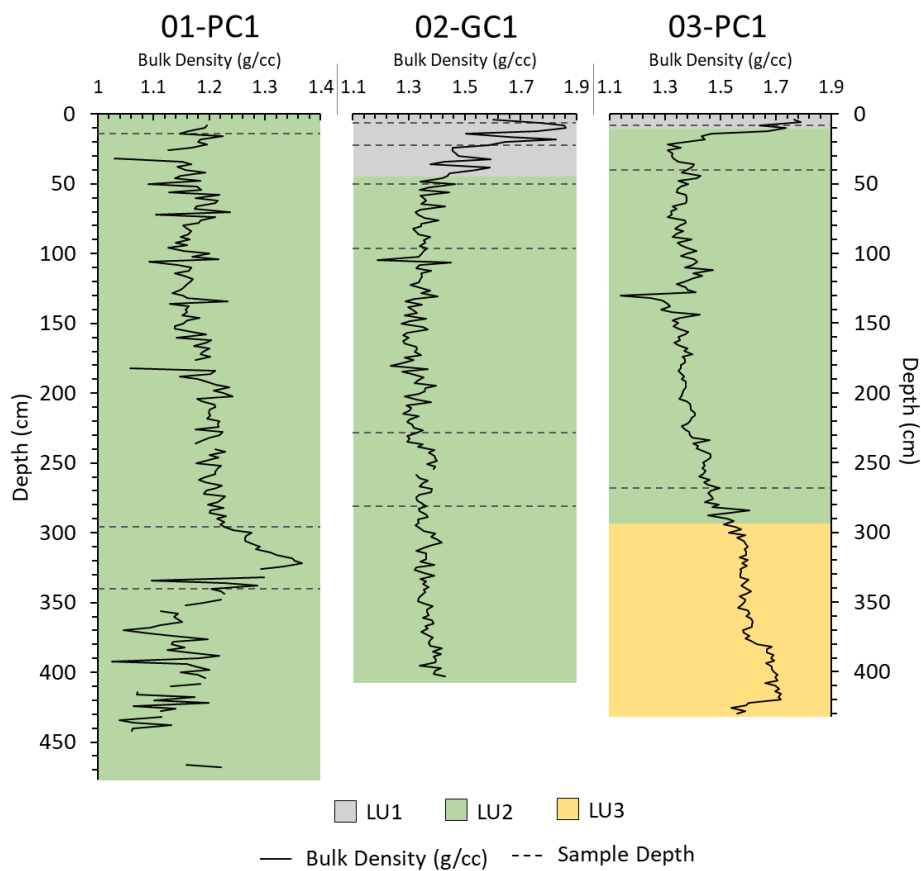


**Figure 5.** Bulk density with colors representing each LU. Black dashed line shows the depth where the samples for radiocarbon dating and LOI were taken.

## 4. Results

### 4.1. Geophysical Results

The gridded bathymetry reveals numerous seafloor bedforms and depth variations from 16 m to 237 m in the surveyed area of the Southern Quark (Figure 6). Signs of current activity can be observed in the northern outlets of narrow passages. Potential erosional channels can also be seen just east and southwest of the  $\sim 0.45 \text{ km}^2$  drift deposit where 01-PC1 is located as well as in the western flank of the mapped area (Figure 7).

The backscatter and ARA statistics both display similar seafloor properties throughout the area with lower intensity and mean between and east of the two ridges as well as in the southeastern flank and northern part. This indicates a seafloor with a soft surface and low reflective ability that is often associated with finer sediment. The ARA analysis demonstrates a similar pattern, with significantly lower resolution, however. Areas with low intensity and mean are categorized as having a high  $\Phi$  value in the ARA analysis, which correspond to a finer grain size (Figure 6). Surface measurements from all six cores reveal that the location of 01-PC1 is finer than the rest, which corresponds with what is seen in the ARA analysis.

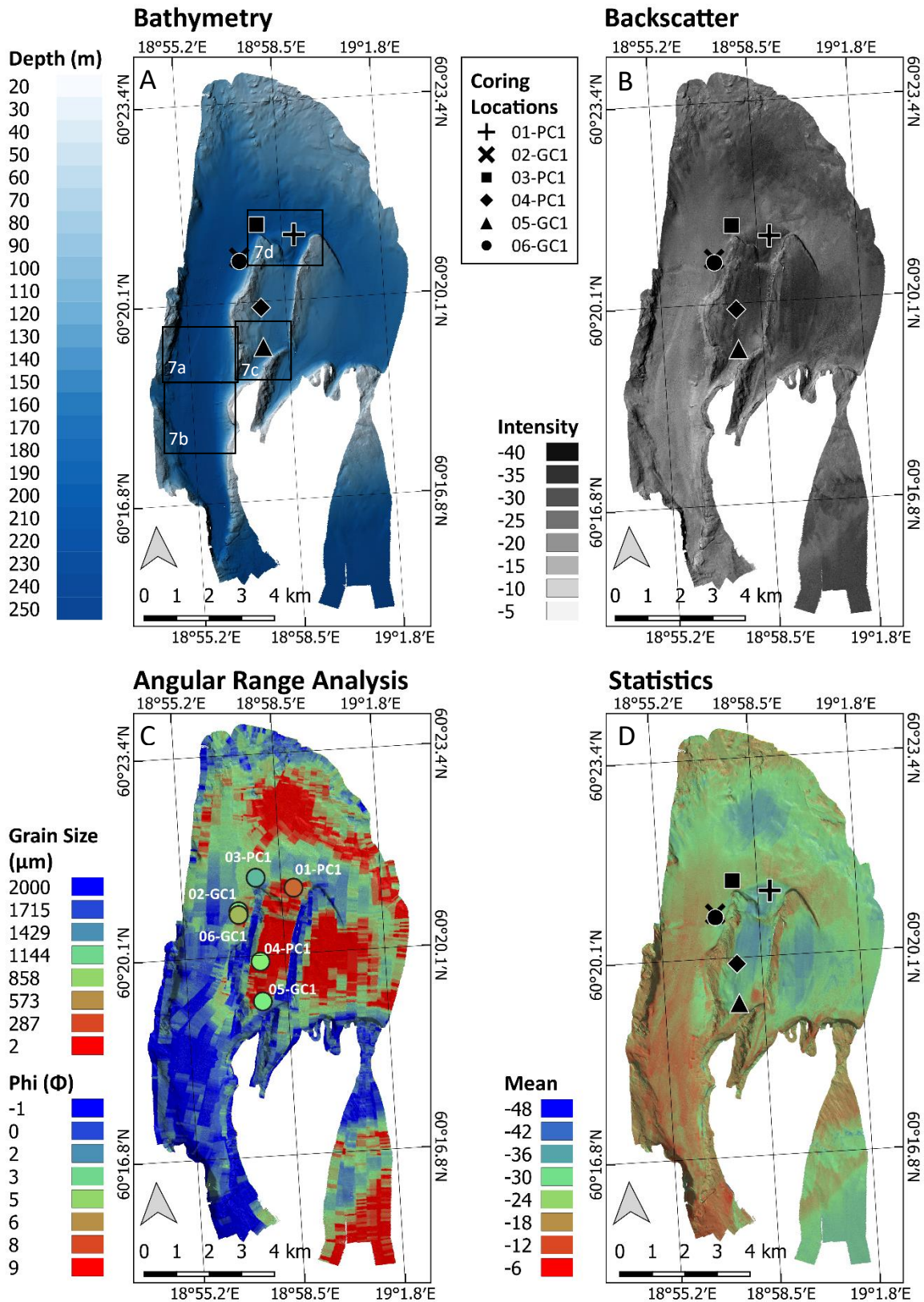


**Figure 6.** Geophysical and statistical results from the survey area. A show the bathymetry with depth reaching down to ~240 m. Squares indicate locations of panels in Figure 7. B displays the backscatter mosaic with a resolution of 0.9x0.9 m. C shows the Phi ( $\Phi$ ) and grain size ( $\mu\text{m}$ ) ARA analysis which is a model representing the approximate surface sediment grain size. Coring locations shows the measured surface grain size at each site, color coded to match the grain size and Phi scale D displays the backscatter statistics with a mean resolution of 18x18 m.

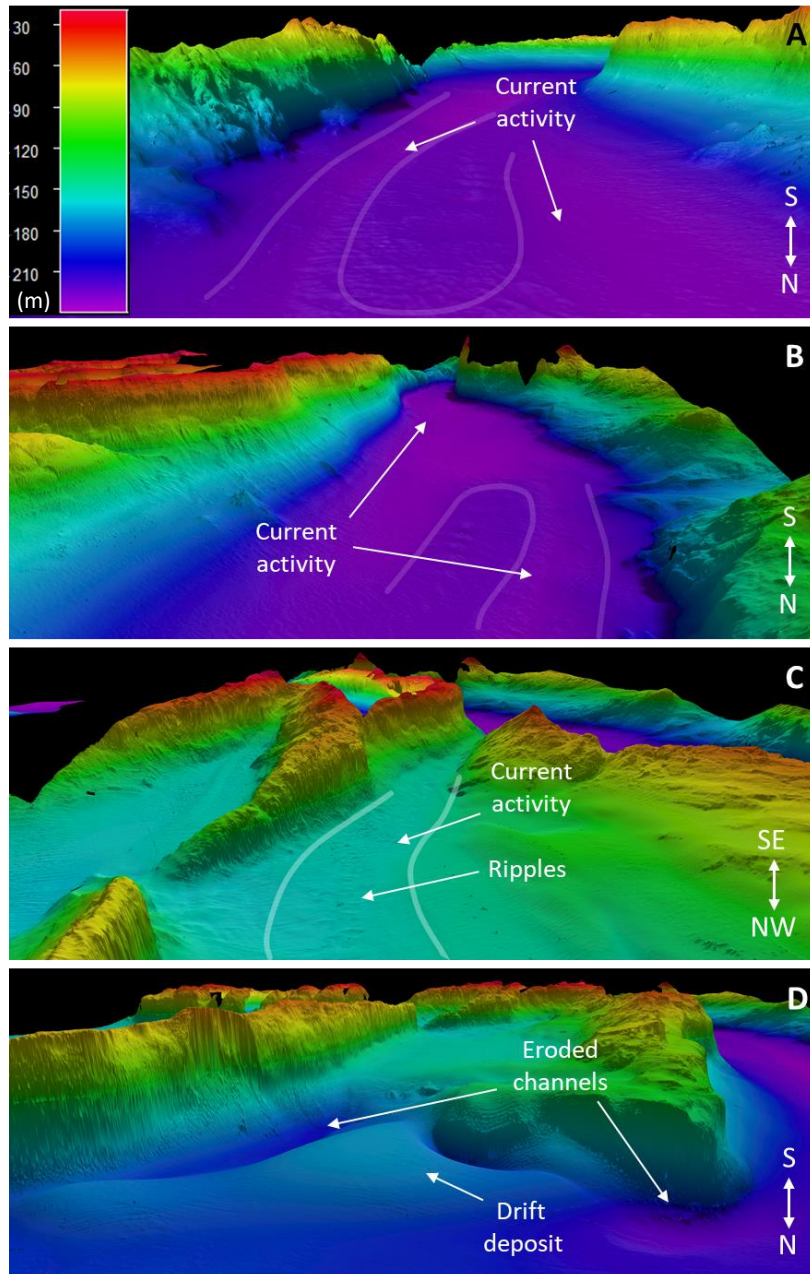


**Figure 7.** 3D views of survey area with a 3x depth exaggeration. A) Signs of current activity in the western flank of the area, looking north. B) Signs of current activity looking south to the outlet of the deep-water passage. C) Ripples created by currents just north of an outlet. D) Eroded channels adjacent to the drift deposit.

#### 4.2. Sub-Bottom Profiles

Much like the interpretation of the multibeam mapping, the SPB's indicate strong current activity in several parts of the survey area. Channels that truncate underlying reflectors are observed just above the northern tips of the two ridges oriented in an E-W direction. These are adjacent to the drift deposit (Figure 8A & 7B). Longer channels oriented in a N-S direction are observed with weaker homogenous acoustic reflectors close to the sea floor in the most western part of the area, adjacent to truncated stronger laminated acoustic reflectors (Figure 8C-7E). These signs of erosion weaken northward as the straits become wider and eventually shallower. The erosional force appears however to be stronger north of the ridges since the channels are more pronounced, and truncation more clearly defined.

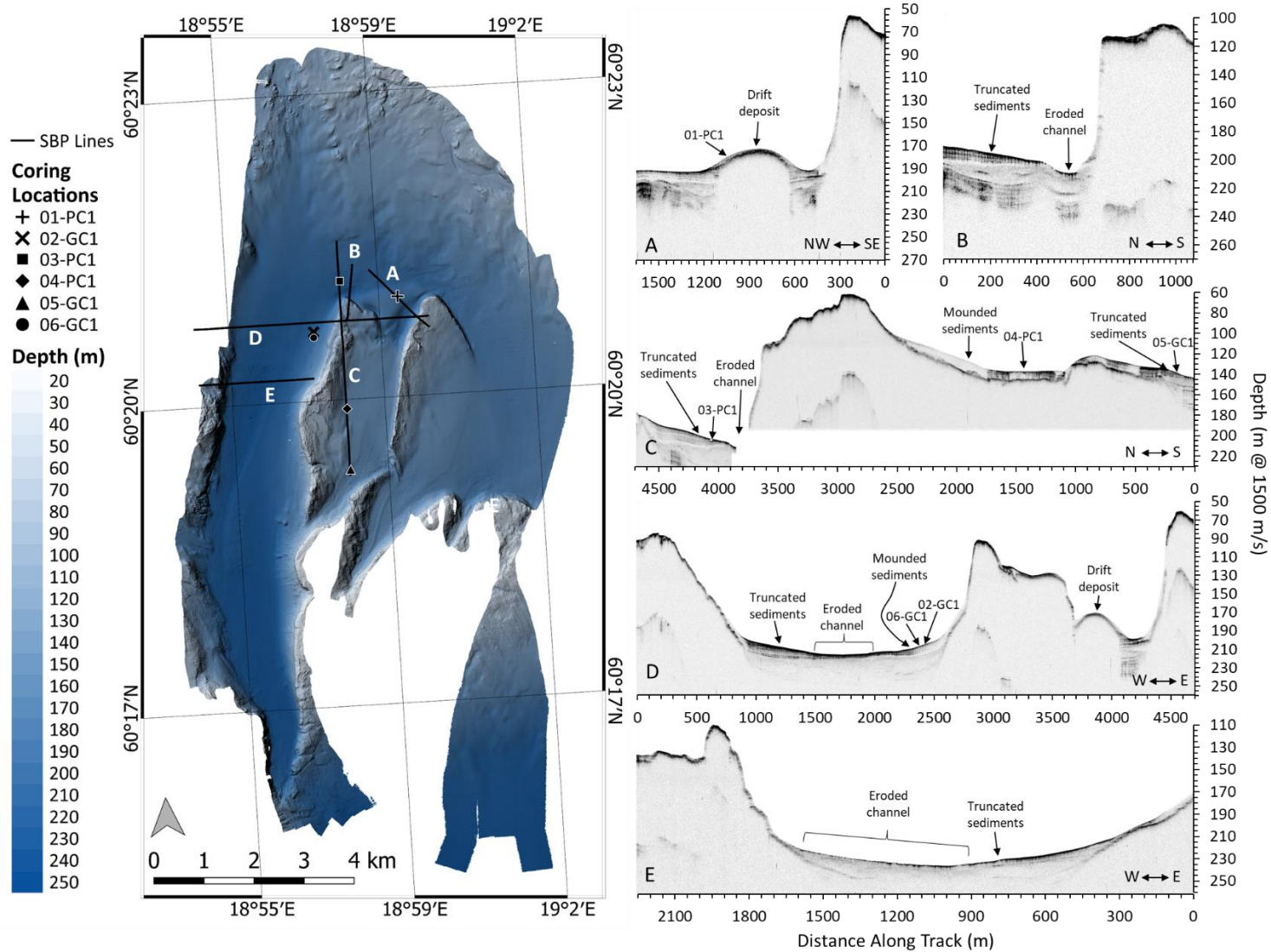


**Figure 8.** Bathymetry with five SBP's marked out to show their location and orientation (left). SBP's with arrows to illustrate the general morphology and common bedforms in the area (right). Brown: eroded channels, green: truncated sediments, blue: drift deposit, purple: mounded sediment (interpretation modified from Holmlund et al., (in press)).

The general appearance of the SBP's show a pronounced seafloor reflector with somewhat developed laminated reflectors underlying it. This is however not seen in every profile due to the large amounts of artifacts and poor resolution of the sub surface caused by factors such as gas-saturated sediments. Parts of the area do show several possible acoustic units with distinct acoustic properties. Correlation between of these units between profiles is however difficult due of the amount current activity, which has eroded and truncated the well-developed reflectors and means that the continuity between reflectors and acoustic units is often interrupted. Similarly, the acoustic basement is clearly visible and easy to interpret in some areas, and in others almost invisible which leads to great uncertainty when compiling a sediment thickness map (Figure 9).

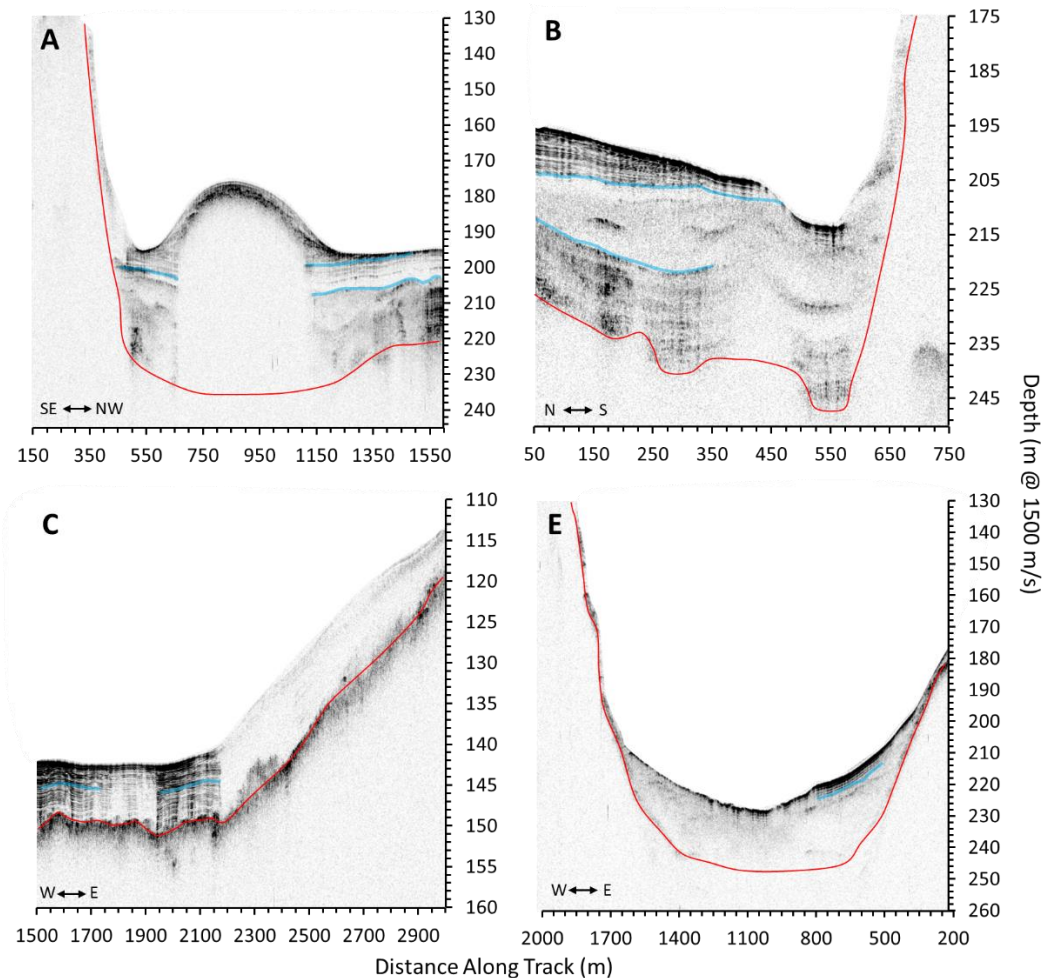


**Figure 9.** Sub-bottom profiles using the same letter coding as Figure 8 to illustrate the general sedimentary facies in the SBP's. Blue lines indicate a possible change of acoustic unit, these have not been mapped out spatially due to the numerous interruptions. The red lines represent the interpreted acoustic basement, which consists of either till or bedrock. C has a clearly defined acoustic basement, while in A and B it is not as pronounced. The acoustic basement in E is difficult to make out.

#### 4.2.1. Sediment Thickness Compilation

A rough compilation of the sediment thickness demonstrates that bathymetric highs possess the lowest amount of sediment accumulation while the deeper basins have a greater accumulation of sediment. The sediment is thickest at the drift deposit where 01-PC1 was collected and towards the east of the survey area. 04-PC1 and 05-GC1 are located on the thinnest sediment cover of the collected cores (Figure 10). The compilation is a rough estimate of the sediment cover and is solely based on the 25 SBP's collected in the nearly 80 km<sup>2</sup> area. The parallel profiles are about 1 km apart. The acoustic basement was manually interpreted from the SBP's, which was poorly resolved in several profiles.

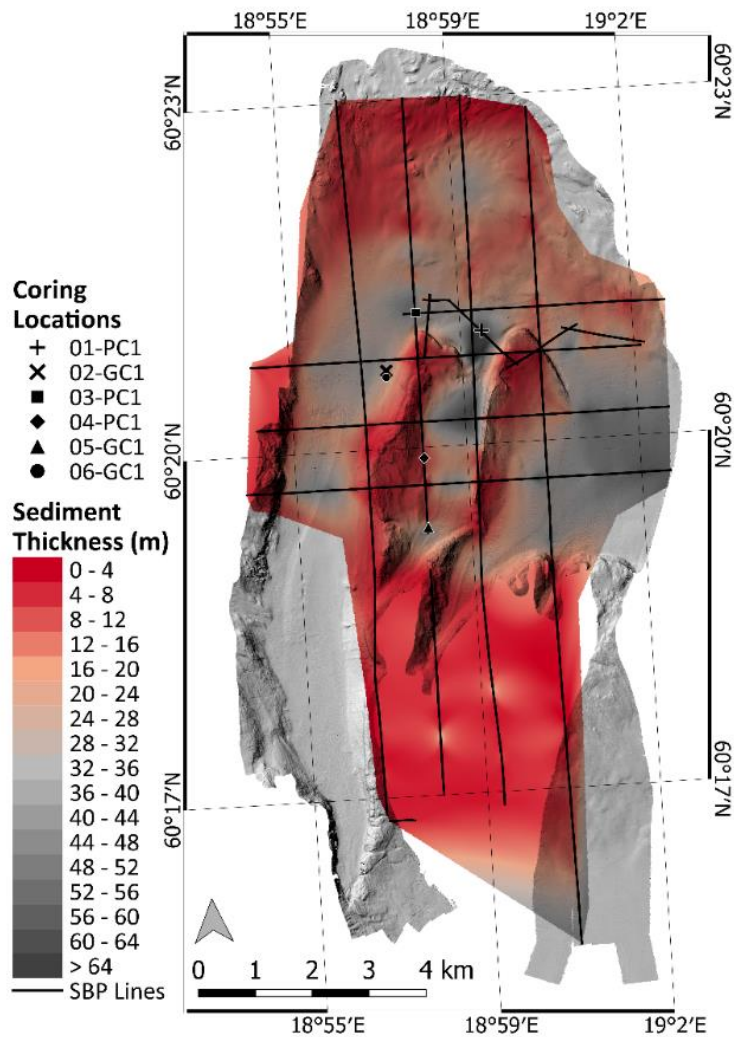


**Figure 10.** Interpolated sediment thickness based on SBP. Thinner sediment (dark red colors) accumulation is generally found in bathymetric highs, while the deeper basins usually have the greatest sediment accumulation. Areas of the NW, NE, SE, and SW part of the map have been removed due to the large uncertainty in those areas. Compiled surface overlies a hill shade of the bathymetry to provide depth perception.

#### 4.2.2. Acoustic Appearance at the Coring Sites

A strong acoustic reflector representing the seafloor is present at each coring site. No laminated acoustic reflectors are visible in the sediment drift deposit where 01-PC1 is located. This is likely due to gas blanking in the sediments (Figure 11A). The site of core 02-GC1 exhibit well developed acoustically laminated reflectors in the west, which eventually fades to a blank subsurface in the east near the rock wall, probably due to interference from soundwaves reflected from the steep bathymetry. Signs of mounded sediments can also be seen in the east around this site (Figure 11D). Evident effects of current erosion are observed close to 03-PC1. Truncated continuous wavy reflectors are seen in the northward going profile (Figure 11C), which appear to more hummocky in the westward going profile (Figure 11BR). The appearance of the two profiles at the site of 03-PC1 are clearer than many other profiles which makes the acoustic reflectors easier to follow. The lithologic unit interpretations somewhat match apparent changes in acoustic units, but these units are too inconsistent between the profiles to attempt to link them regionally.

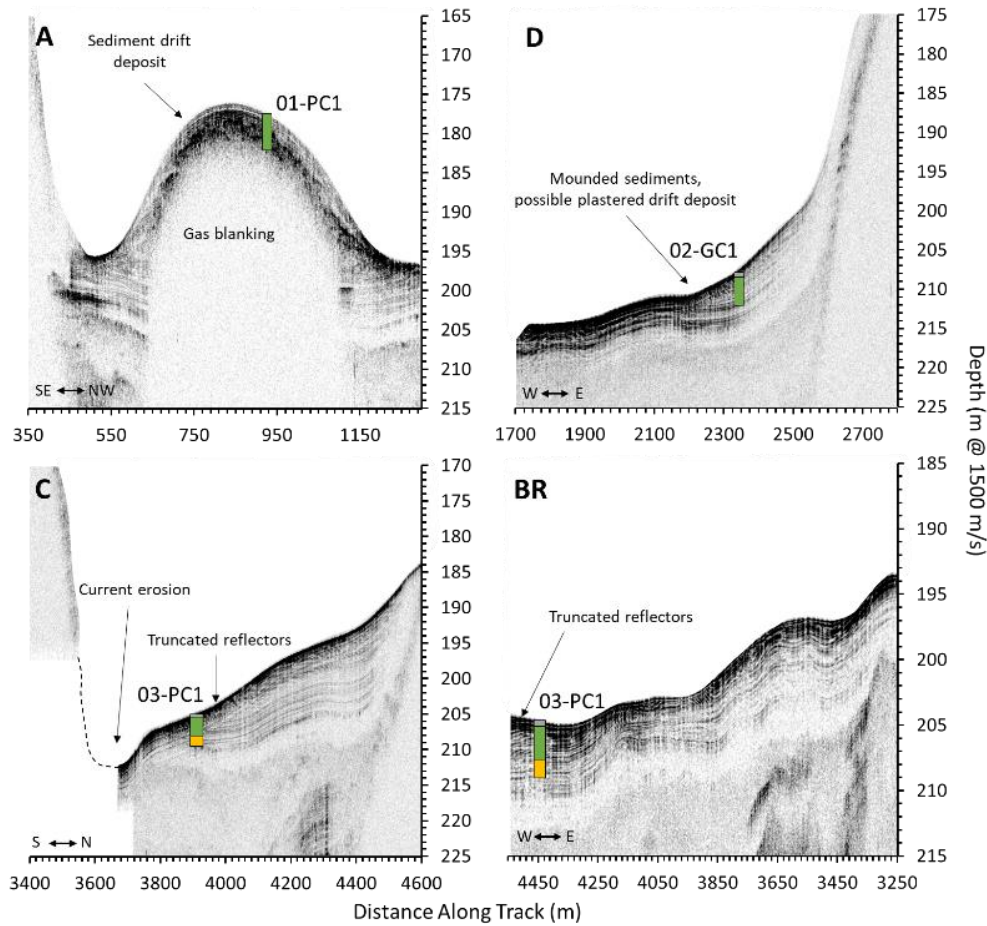


**Figure 11.** SBP's with interpretations and coring locations marked out for the further investigated cores. Same letter coding is used as in Figure 8 except from the bottom right (BR) profile which is not emphasized in that figure. This profile crosses profile C right at the coring site in a W – E direction. Colors represent the rough LU boundaries based on the core descriptions. Grey: LU1, Green: LU2, Yellow: LU3 (LU and SBP interpretations from Holmlund et al., (in press) ). It should be noted that 02-GC1 is projected on to the SBP in D because it was collected roughly 190 m south of the SBP in the figure.

#### 4.3.LOI

Loss on ignition revealed that OC varied between 1 and 7 % (Figure 12). Lower values were generally observed close to the sea floor in LU1 or near the boundary to LU2 with higher contents of OC deeper in LU2. Core 01-PC1 showed the highest average LOI value of 5.9%, followed by 02-GC1 with 3.9% and 03-PC1 with 3.4% (Appendix A).

From the 3 samples that were taken in 01-PC1, the OC content appears to increase with depth accounting for 5.4% of the sample at 14 cm and increasing to 5.9% at 296 cm. The third sample was taken at 340 cm, just below the 0.2 g/cc increase in bulk density (Figure 12, 01-PC1) and had the highest OC content of 6.5%.

In 02-GC1, the organic carbon content increase sharply from 1.3% at 6 cm to 5.3% at 96 cm. Two measurements in between showed 2.4% at 22 cm and 4.3% at 50 cm. The remaining samples remain relatively constant at 4.8% (228 cm) and 4.9% (280 cm).

Despite only half as many measurements compared to 02-GC1, the OC follows a similar trend in 03-PC1. At 8 cm the OC content is 1.8% and increases to 3.5% at 40 cm. The deepest sample was taken at 268 cm and contained an OC content of 4.9%.

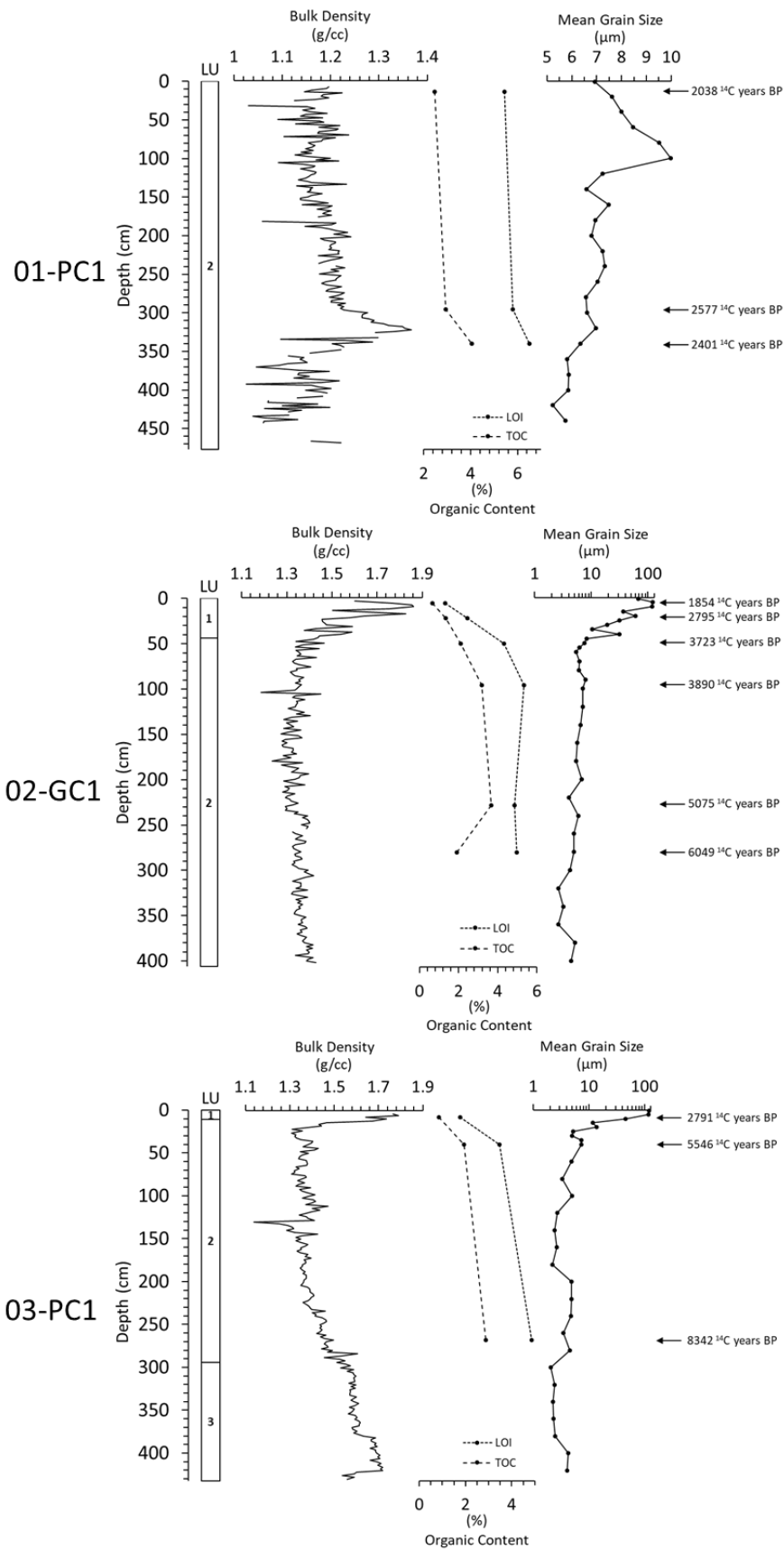


**Figure 12.** From left to right: Lithologic Unit (LU), bulk density from MSCL data, organic content (both LOI and TOC), mean grain size calculated with the GRADISTAT excel plugin (v.9.1) from Blott and Pye (2001) using the Folk and Ward (1957) method (note the log-scale for 02-GC1 and 03-PC1 compared to the narrow range of variability in the linear scale for 01-PC1), positions and uncalibrated ages (<sup>14</sup>C years) of dated samples are shown with arrows.

#### 4.4. Radiocarbon Dating and TOC

Radiocarbon ages acquired from the 12 samples of 01-PC1, 02-GC1 and 03-PC1 show downcore progression towards older ages in all cores (Table 3). Ages from 01-PC1 show little variation between the three samples that were dated, with one possible age reversal just above 3 m. With a total age range of 500 <sup>14</sup>C years in 3.4 m of sediment, the rate of deposition (6.8 mm/yr) appears to have been much higher than the two remaining cores (Figure 12, 01-PC1). Six dates were obtained from 02-GC1 that displayed a larger age range of 4200 <sup>14</sup>C years with no apparent age reversals. The sedimentation rate should then be 0.66 mm/yr assuming a linear rate of deposition (Figure 12, 02-GC1). 03-PC1 had the slowest assumed linear rate of deposition of 0.49 mm/yr and largest age range of 5500 <sup>14</sup>C years based on three samples. This core also contained the oldest dated sediment with an age of ~8300 <sup>14</sup>C years BP (Figure 12, 03-PC1).

The pattern of TOC values measured on the elemental analyzer at ETH-Zürich follows the LOI measurements closely, being roughly 0.5 times the LOI OC content. One notable exception is the deepest sample in 02-GC1 that decreases 1.75% while the value for the LOI slightly increases (Figure 12, raw values in Appendix A).

**Table 3.** Data from the bulk radiocarbon dating. Light grey section is the calibrated radiocarbon age using the *calib.org* website version 8.20, which used calibration datasets from (Reimer et al., 2020). Dotted horizontal lines separates the three cores.

ETH nr.	Sample ID	Depth (cm)	LU	F <sup>14</sup> C	+ - (%)	age (y)	+ - (y)	C/N ratio	δ <sup>13</sup> C (‰)	cal median age (y)	cal 2σ min (y)	cal 2σ max (y)
121257.1.1	DATE-1PC-1-0,14m	14	2	0.776	0.869	2038	70	5.3	-25.11	1985	1723	2268
121258.1.1	DATE-1PC-3-1,175m	296	2	0.726	0.894	2577	72	4.91	-24.07	2635	2371	2846
121259.1.1	DATE-1PC-4-0,11m	340	2	0.742	0.900	2401	72	5.9	did not work	2475	2331	2719
121251.1.1	DATE-2GC-1-0,06m	6	1	0.794	0.852	1854	68	4	-25.58	1767	1588	1932
121252.1.1	DATE-2GC-1-0,22m	22	1	0.706	0.873	2795	70	4.5	-24.7	2906	2757	3103
121253.1.1	DATE-2GC-1-0,5m	50	2	0.629	0.897	3723	72	5.2	-25.29	4074	3850	4344
121254.1.1	DATE-2GC-1-0,96m	96	2	0.616	0.918	3890	74	6.5	-25.85	4311	4092	4520
121255.1.1	DATE-2GC-2-1,24m	228	2	0.532	0.993	5075	80	7.6	-25.64	5810	5603	5990
121256.1.1	DATE-2GC-3-0,245m	280	2	0.471	1.044	6049	84	4.7	-26.21	6906	6680	7159
121260.1.1	DATE-3PC-1-0,08m	8	1	0.707	0.953	2791	77	4.45	-25.15	2905	2754	3139
121261.1.1	DATE-3PC-1-0,4m	40	2	0.501	0.977	5546	79	5.38	-26.44	6346	6128	6498
121262.1.1	DATE-3PC-2-1,385m	268	2	0.354	1.124	8342	90	10.12	-27.64	9336	9034	9528

## 4.5. Grain Size

### 4.5.1. Surface Sediment

Surface sediment grain size measurements show that 01-PC1 contains the finest material with a silt content of roughly 70%. The remaining five cores had considerably coarser material with sand around 100-200  $\mu\text{m}$  as the dominant component. Which is consistent with the visual core descriptions that noted an uppermost lithologic unit at each of the remaining sites that had a sandy texture. Core 05-GC1 contained the coarsest grains  $>400 \mu\text{m}$ , but 03-PC1 had the most abundant sand content at the surface (84%) (Figure 13).

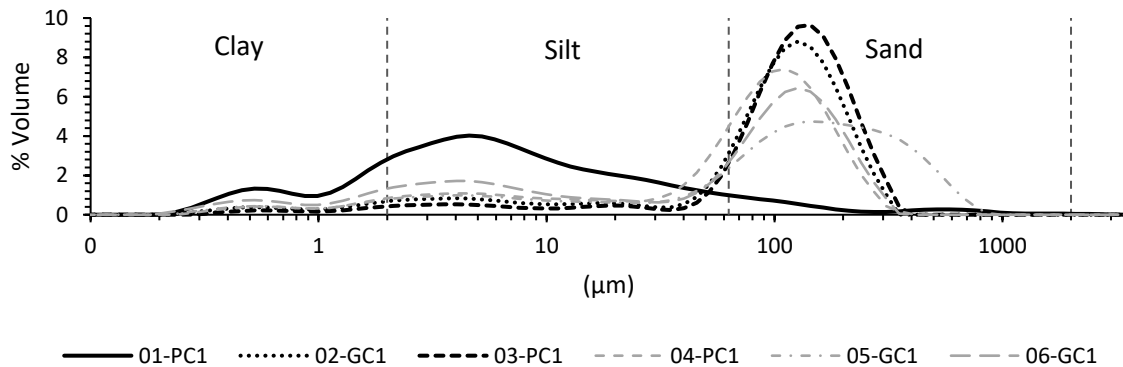


**Figure 13.** Surface grain size distribution of all six cores that were collected on expedition EL17-IGV04. Black thick lines represent the cores which were further investigated, thin grey lines represent the rest of the cores. All organic content had been removed prior to the grain size analysis. Grain size classification modified from Udden, (1914) & Wentworth (1922).

### 4.5.2. Downcore Grain Size

Sediment in the three cores were predominately fine silt, occasionally overtaken by clay. 01-PC1 had a generally constant grain size distribution throughout the whole core with a slight brief increase of sand around 1 m (Figure 14, 01-PC1). Core 02-GC1 exhibited a more varied size distribution downcore. Unlike 01-PC1, 02-GC1 has an uppermost unit consisting almost entirely of sand, which gradually transitions to a more clay and fine silt rich composition in LU2. The Sortable Silt fraction is most abundant from 50-200 cm and gradually decreases below this point as clay and fine silt increases (Figure 14, 02-GC1). LU1 in 03-PC1 also has a seafloor grain size dominated by sand with no more than 20% clay, fine silt and sortable silt combined. The transition to finer sediment is however sharper than the previous core and shifts to a majority of clay and fine silt just below the boundary to LU2 (11 cm). Abundance of finer grains increases gradually down to 120 cm where it remains fairly constant with almost no sand until 180 cm where sand content rises. This period of increased sand content continues down to 300 cm, just after the boundary to LU3, where it largely disappears, and a sharp rise in fine silt is observed. This ratio of grain sizes remains constant until 400 cm where sortable silt content increases to almost 20% where it remains to the bottom of the core (Figure 14, 03-PC1).

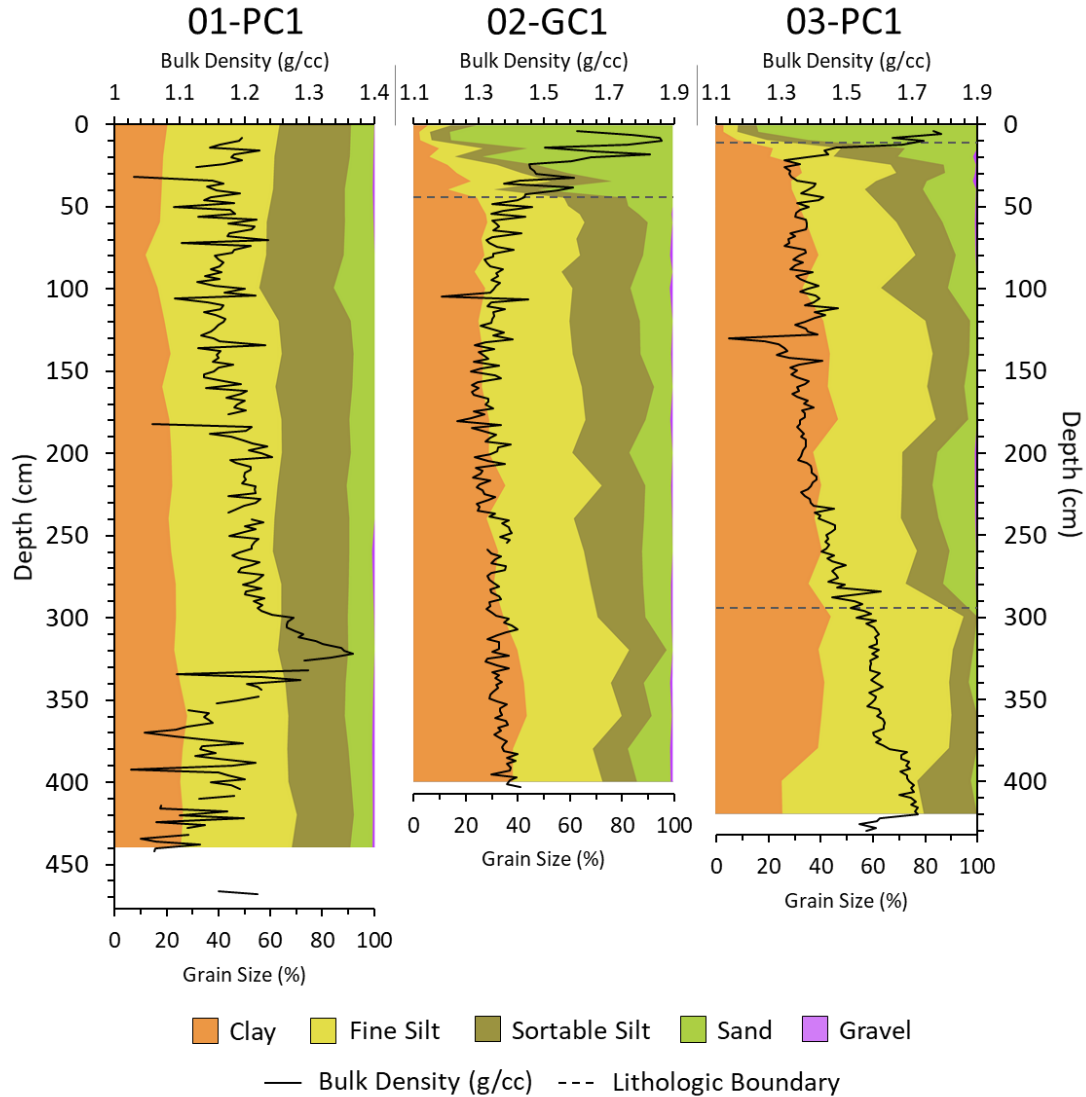


**Figure 14.** Downcore grain size measurements from the three cores. Sampling resolution was based on the variations in the bulk density data. Resolution; 01-PC1: 20 cm down to 440 cm. 02-GC1: 5 cm down to 60 cm, thereafter 10 cm down to 100 cm, then 20 cm down to 400 cm. 03-PC1: 5 cm down to 40 cm, thereafter 20 cm down to 420 cm (Appendix B). Grain size classification; Clay:  $<2\mu\text{m}$ , Fine Silt:  $2\text{-}10\mu\text{m}$ , Sortable Silt:  $10\text{-}63\mu\text{m}$ , Sand:  $63\mu\text{m} - 2\text{mm}$ , Gravel:  $2\text{-}3.5\text{mm}$  (grain size classification modified from Udden (1914) & Wentworth (1922), where the sortable silt range is according to McCave et al. 1995). 01-PC1 is only classified as LU2, 02-GC1 is classified as LU1 and LU2 where the dashed line marks the lithologic boundary, 03-PC1 is classified as LU1, LU2 and LU3 where the dashed lines mark the lithologic boundaries.

#### 4.5.3. SS% and $\overline{\text{SS}}$ correlation

Two of the three cores that were analyzed for their sortable silt ratio displayed and increase in  $\overline{\text{SS}}$  with increased SS% (Figure 15). This is diagnostic of current sorted sediments. Core 01-PC1 did not display a strong linear relationship and were clustered between 23-35 % and  $20\text{-}24\mu\text{m}$  (Figure 15A). 02-GC1 displayed the strongest linear correlation with a slope of  $\sim 0.3$  ( $R = 0.91$ ) for all samples from the core (Figure 15C). Unlike 01-PC1, 02-GC1 is categorized into two lithologic units (LU1 & LU2) that appear to differ in both slope and correlation. LU1 has a steeper slope and larger R value ( $\sim 0.3$  and  $0.93$ ) respectively with a total of 9 measuring points, while LU2 has 23 measuring points with a slope of  $\sim 0.15$  and R of  $0.74$  (Figure 15D). The whole core of 03-PC1 does not exhibit as good correlation as the previous core ( $R = 0.85$ ), but has a larger slope of  $\sim 0.4$  (Figure 15E). Much like the previous core, the lithologic units appear to have separate relationships between  $\overline{\text{SS}}$  and SS%. LU1 contains the largest size and highest abundance of grains in the sortable silt range, and with 3 measuring points it possesses the

lowers R of 0.71 and a slope of  $\sim 0.27$ . With 18 measuring points, LU2 has the highest R value of  $\sim 0.87$  and a  $\sim 0.27$  slope. LU3 contain the lowest amount as well as the smallest size of the sortable silt range and a distinctly shallower slope of  $\sim 0.12$  than the other units. This unit consists of 7 measuring points and has a linear correlation coefficient of  $R = 0.82$  (Figure 15F).

All three cores have LU2 as their common denominator, and the properties of this unit appears to be constant between the cores (except for the slope and R value in 01-PC1). The  $\overline{SS}$  ranges between  $\sim 20$  and  $\sim 28 \mu\text{m}$ , being most abundant between 20-25  $\mu\text{m}$  and the SS% within this size range varies between 10-36% in all cores (Figure 16).

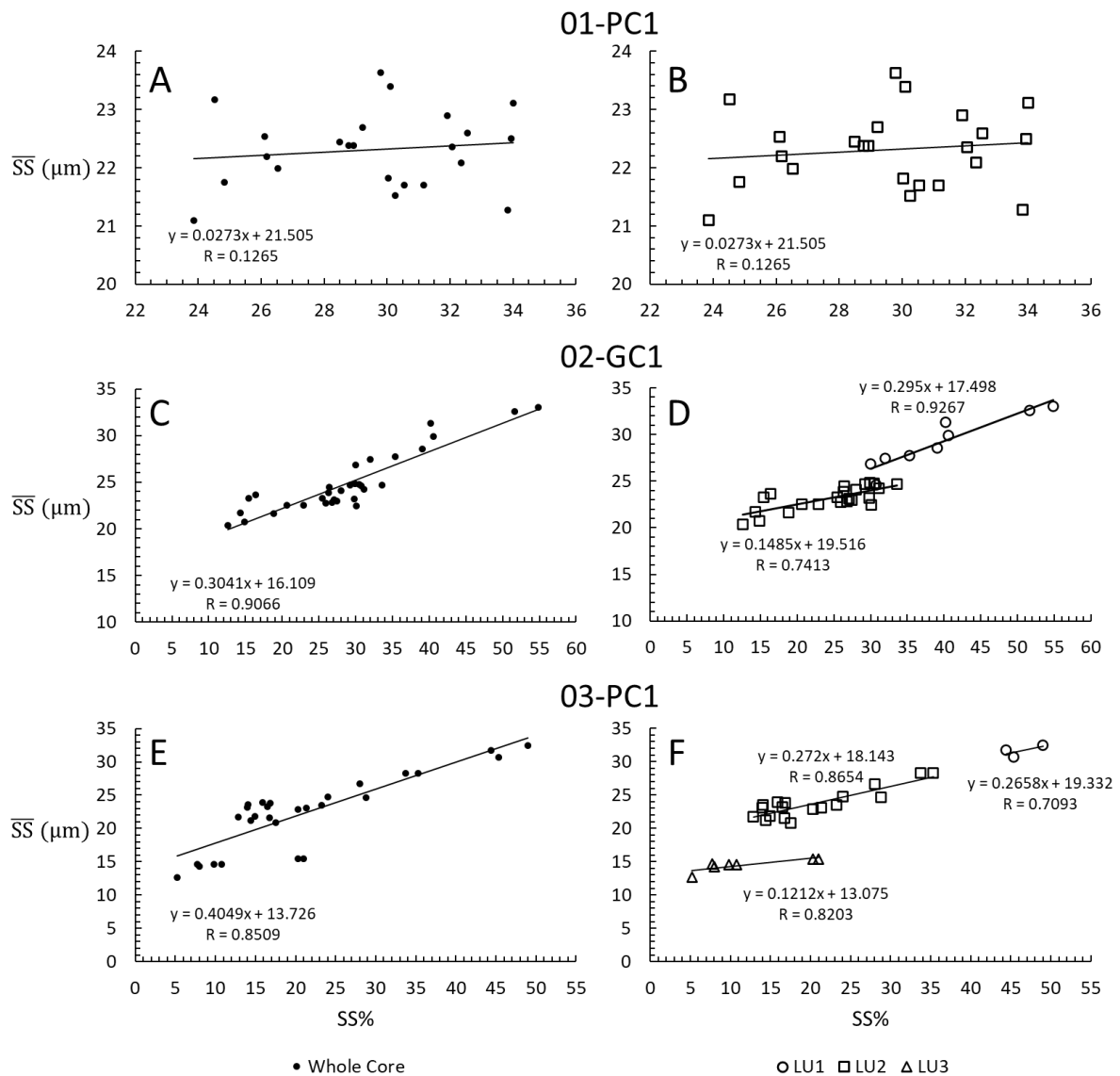


**Figure 15.** SS% vs  $\overline{SS}$  plots of cores 01-PC1, 02-GC1 & 03-PC1. A, C & E shows results from the whole core. B, D & F are categorized based on the lithologic units. A & B show no significant relationship between SS% and  $\overline{SS}$ . C - F appear to display a significant relationship in both whole core and individual lithologic units.

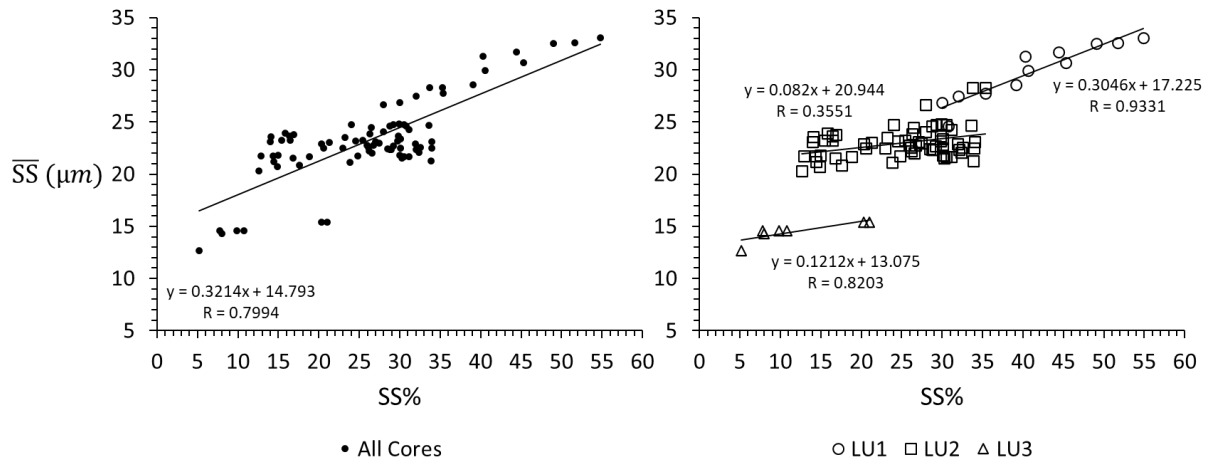


**Figure 16.** SS% vs  $\overline{SS}$  of all three cores. Illustrates that the lithologic units have similar properties in terms of sorting regardless of core location. LU2 has a lower correlation combined than 02-GC1 and 03-PC1 have individually. It is most likely 01-PC1 that lowers the overall correlation. Since LU2 is so clearly defined in 02-GC1 and 03-PC1, and 01-PC1 falls within their range, the sediment could still be current sorted.

## 5. Discussion

### 5.1. Current Controlled Sedimentation

The seafloor of the Southern Quark has been heavily influenced by current activity. This is evident by the channels, ripples and sediment drifts seen in the bathymetry (Figure 8). Similar indications are observed in the sub-bottom data where channels are incised into the sediment and truncate underlying reflectors. This is further supported by sedimentological observations, where a coarse sandy unit (LU1) cap 2 of the 3 examined cores and is noted in 5 of the 6 recovered core descriptions (01-PC1 being the exception). Depending on the current strength, it has the potential to re-suspend, erode, or deposit sediment of different sizes. (McCave et al., 2017, 1995).

It is the correlation between SS% and  $\overline{SS}$  that indicate if the sediment is current sorted or not. Reliable values for correlation coefficients of well sorted sediments have shown been to be  $R > 0.5$  (McCave and Andrews, 2019). All units in the examined cores (except LU2 in 01-PC1) appear to be current sorted since they show  $R \geq 0.7$ . In their 2017 paper, McCave et al., inferred paleo-flow speeds based on sediments from the Iceland overflow region in the  $\overline{SS}$  range. Variations in grain size between 18 to 30  $\mu\text{m}$  indicated flow speeds between 5 to 20  $\text{cm s}^{-1}$  that had a slope of  $0.81 \mu\text{m}/\text{cm s}^{-1}$ . In 02-GC1 and 03-PC1 the correlation between SS% and  $\overline{SS}$  exceeds the criterion for being reliability sorted in LU2 and lies within the same  $\overline{SS}$  range as McCave et al., (2017). However, to say whether these estimated current speeds are reasonable for the surveyed area is too uncertain since it is two completely different sites. However, their results do provide a rough estimate on what velocities could be associated with the 18 – 30  $\mu\text{m}$   $\overline{SS}$  range. Laboratory studies performed in 2020 explored the SS hypothesis and set out to relate flow speeds to grain size sorting. Exposing sediment to typical deep se current velocities of 5-25  $\text{cm s}^{-1}$ , the study found that the slope relationship between the velocity and the size was dependent on the distance between the outlet of the current and the location of interest. The  $\overline{SS}$  size reduces further from the outlet and when exposed to higher current velocities (Culp et al., 2020). The ARA analysis suggests a very coarse-grained region in the south-western part of the survey area at the deep-water passage highlighted in Figure 1, which may be interpreted as the outlet for the currents that shaped the current channels and drift deposit.

Other studies suggest that the SS proxy is used as a measure for size sorting by selective deposition in flow speeds below 10 – 15  $\text{cm s}^{-1}$ . Velocities above that range cause winnowing of finer materials as well as selective deposition (McCave and Hall, 2006). This lies within the range of observed northward bottom currents in the Understen-Märket trench of 14 to 98  $\text{cm s}^{-1}$  (Ambjoern and Gidhagen, 1979;

Hietala et al., 2007; SMHI, 2021). The capped unit of coarser grains found in our cores (LU1), along with evidence of erosion in the bathymetry and SBP's also indicate that the survey area has experienced current speeds capable of removing fines from the seafloor.

## 5.2. Sediment Age & Stratigraphy

Dating of marine sediments can in many parts of the Baltic be problematic as carbonate microfossils commonly used for radiocarbon dating are absent. An alternative approach is to date the organic carbon in the bulk sediment (Moros et al., 2020). This method can however be challenging, as the bulk sediment can both have a marine and terrestrial component. Marine OM more likely reflects primary productivity at the time of deposition. Terrestrial OM or reworked marine components may be older OM and thus not reflect the depositional age (Lougheed et al., 2013; Possnert, 2001). Moros et al., (2020) separated these fractions in cores from the Gotland Basin within the Baltic and compared it to the bulk ages. He found that the bulk ages matched relatively well with the base-extractable and base-insoluble (marine and terrestrial components respectively) components in laminated sections of the core with a high TOC. In homogenous sections, the marine fraction provided better results where the terrestrial components tended to overestimate the age by about 1000 – 3000 <sup>14</sup>C years.

Here we only dated the bulk sediment. The  $\delta^{13}\text{C}$  to  $\text{C}/\text{N}$  ratio, which can be used to discriminate the source of the material, shows that most samples are marine to freshwater algae (Figure 17). One outlier being the deepest and oldest sample from core 03-PC1 which showed a more dominant freshwater algal origin.

The Baltic has undergone 5 stages since the last deglaciation: Baltic Ice Lake, Yoldia Sea, Ancylus Lake, Littorina Sea and present Baltic/Post Littorina (e.g. Andrén et al., 2000; Winterhalter et al., 1981), that have been relatively well dated. Each stage is associated with unique environmental conditions that are reflected in the sediment lithology. The Baltic Ice Lake is for example characterized by varved glacial clays with varying thicknesses deposited during the retreat of the ice sheet. The lowermost sediment (LU3) in 2 of the 6 cores retrieved from the survey (01-PC1 and 05-GC1) somewhat resembled this description of glacial clay (Holmlund et al., in press). Without

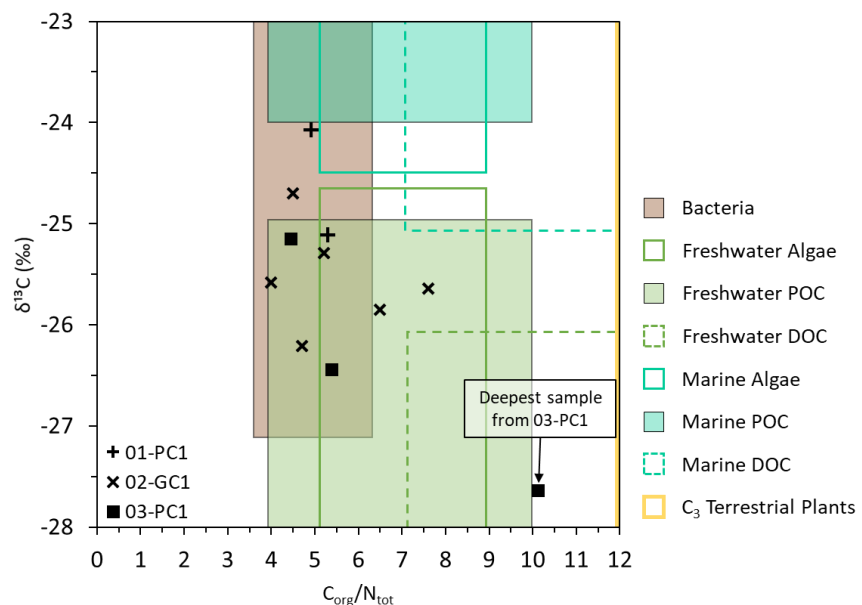


**Figure 17.**  $\delta^{13}\text{C}$  plotted against  $\text{C}_{\text{org}}/\text{N}_{\text{tot}}$  from the dated samples (deepest sample from 01-PC1 did not work). Black arrow pointing to deepest and oldest sample from 03-PC1. Colored and squared areas mark the typical ranges for different carbon sources. POC: Particulate Organic Carbon, DOC: Dissolved Organic Carbon (modified from Lamb et al., 2006; and references therein).



**Figure 18.** Images of core 03-PC1 and 05-GC1 showing black sulfide bands just below sulfide stains. Note the different depths in the core, and that the cores are collected approximately 3.8 km apart.

winning at 02-GC1 and 03-PC1. If this is the case, the oldest age from 01-PC1 should be younger than the onset of current scouring. This is supported by the raw  $^{14}\text{C}$  age as well as the calibrated  $^{14}\text{C}$  age (Figure 19). The age of sediments observed in 01-PC1 are younger than the LU1/LU2 transition in the other 2 cores supporting the hypothesis that the onset of drift accumulation occurred as currents started to scour the seafloor. According to the estimated timings for the different stages of the Baltic, this change occurred near the Littorina to Post Littorina transition (Figure 20). One problem is that the shallow samples in 01-PC1 are quite old (2-3 kyr BP). This suggests that the bulk OM contained pre-aged carbon and creates some uncertainty on whether the ages from 02-GC1 and 03-PC1 are reliable. However, these older ages at 01-PC1 may be due to re-deposition of material eroded from 02-GC1 and 03-PC1. Samples have been recovered and dried to perform more complex compound specific dating of terrestrial and marine components in the sediment using isotopic dating of  $^{210}\text{Pb}$  and  $^{137}\text{Cs}$ . This have not been performed in the current study but will have to be continued in future work. The  $C_{\text{org}}/N_{\text{tot}}$  vs  $\delta^{13}\text{C}$  cross-plot does not show any significant shift in in the source OM between the three cores (Figure 17), possibly suggesting the old age in 01-PC1 may be the result of reworked locally deposited material. This would remain consistent with our hypothesis that drift sedimentation began synchronously with channel scouring.

dating this part of the sediment though, attributing LU3 to the BIL is too uncertain. Radiocarbon dates of LU2 indicate these sediments were deposited during the Littorina and post Littorina Sea stage – a period characterized by warmer temperatures, more inflow if saline oceanwaters from the North Sea which favored primary production. This is reflected in the sediments high OM and spongy texture (Winterhalter, 1992).

The deepest dated sample from core 03-PC1 falls into the estimated age for the onset of the Ancylus lake or end of the Yoldia Sea stage. The sediment at this depth in the core was grayish green, with black mottling overlying a distinct black band (Figure 18). These features are similar to those attributed to Ancylus lake sediments, deposited during a complex period with increased melting during ice sheet retreat and isostatic uplift. Sporadic pulses of inflowing saline oceanwater caused stratification that developed a strong halocline. Intervals of anoxic bottom waters was interspersed with times of reduced saline inflow increased freshwater and seasonal mixing (e.g. Andrén, 2012; Wastegård et al., 1995; Winterhalter, 1992).

One hypothesis is that the sediment drift deposit at site 01-PC1 started to from when the current strength increased and caused

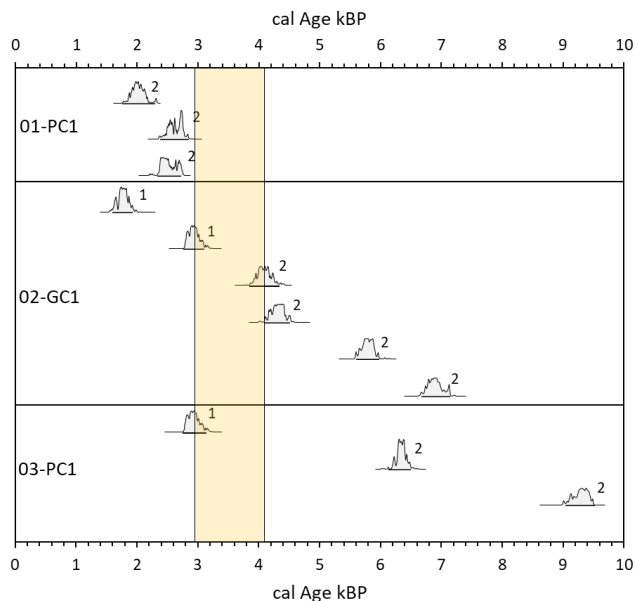


**Figure 19.** Calibrated  $^{14}\text{C}$  age in thousands of years. Yellow bar mark the approximate range of potential ages for the onset of LU1 which is associated with enhanced current strength. All ages in 01-PC1 are younger than this. Numbers indicate LU.

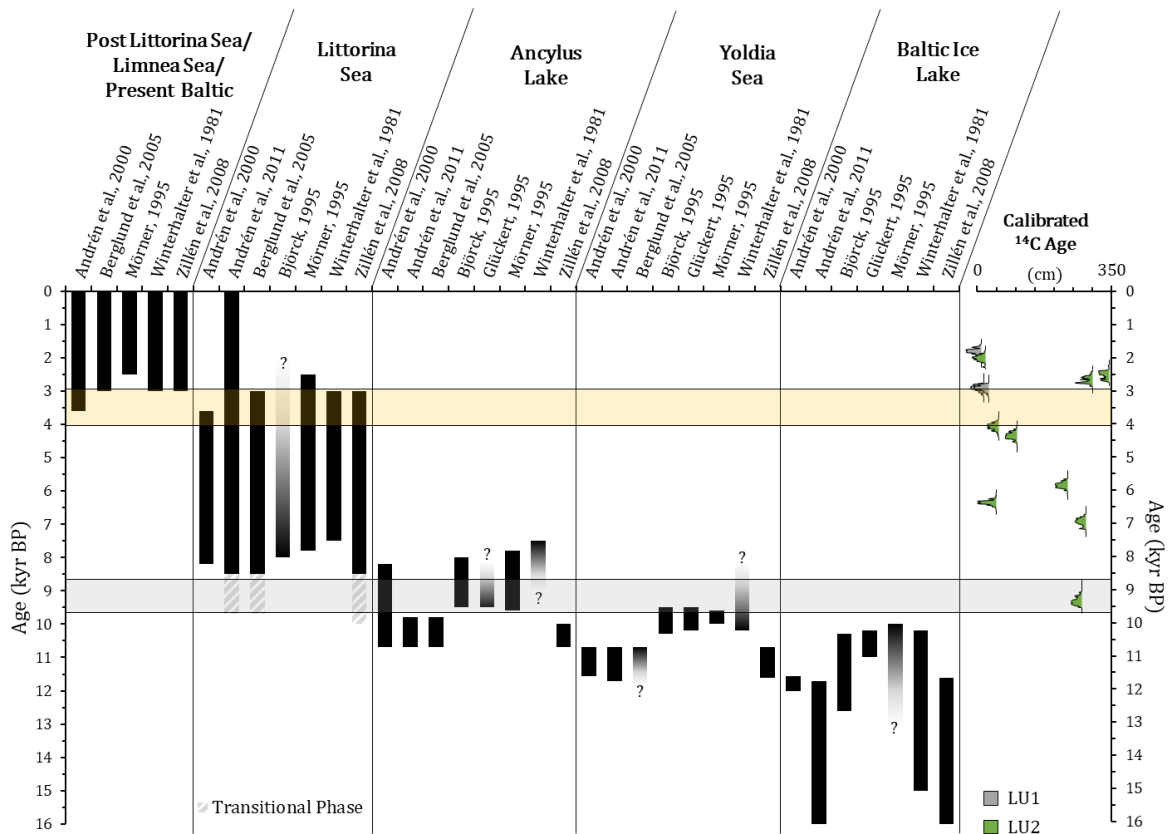


**Figure 20.** Timings of the Baltic Sea stages since the last deglaciation according to several authors (Andrén et al., 2000, 2011; Berglund et al., 2005; Björck, 1995; Glückert, 1995; Mörner, 1995; Winterhalter et al., 1981; Zillén et al., 2008; and references therein). With calibrated  $^{14}\text{C}$  dates on the far right. Faded vertical bars with question mark indicate a specified start point and unspecified end point (or vice versa) by that author. Striped, grey bars indicate an explicit transitional phase between two sea stages. Yellow horizontal bar marks the approximate age of a shift in water transfer to allow for the deposition of sediment found in 01-PC1. Grey horizontal bar indicates the age of the deepest sample collected from 03-PC1 and shows that it roughly lines up with estimated timings of the Ancylus Lake stage.

### 5.3. Environmental Conditions at the Onset of the Post-Littorina Sea

Environmental changes have affected the Baltic Sea throughout the Holocene. The transition from LU2 to LU1 in the sediment cores from the Southern Quark appeared to occur between 4000 – 3000 cal  $^{14}\text{C}$  years BP, at the transition from the Littorina Sea to the Post Littorina Sea. Before this shift, approximately 6.5 kyr BP, the sea level rose by about 5 m in the southern basin, deepening the sills in the Danish strait allowing increased inflow of saline oceanwater (Andrén, 2012; Berglund et al., 2005; Björck et al., 2008). This inflow resulted in the highest salinity in the Baltic during the Holocene (ca. 4% higher than present conditions), which coupled with warmer climate contributed to higher primary production and increased biological activity (Björck et al., 2008; Donner et al., 1999). Increasing salinity also resulted in a stratified water column that reduced vertical mixing and favored hypoxic conditions in water depths >100 m (Sohlenius et al., 2001). After 6000 cal  $^{14}\text{C}$  years BP, salinity started to decrease, and rising sea level was overtaken by the rate of isostatic rebound. This resulted in shallower sills that restricted the inflow of deep saline oceanwater to several basins within the Baltic, especially in the Bothnian Sea and Bothnian Bay (Björck et al., 2008). Paleobathymetric reconstructions of the Baltic during the late Holocene show that the sills in the Åland Sea were substantially deeper 4 – 8 kyr BP. This would suggest that the shallowing, or some threshold was crossed roughly 4 kyr BP, which is close to the timing we infer for the onset of increased current strength. The depth in the Åland Sea shallowed roughly 40 m between 8 to 4 kyr BP, and another 10 m since 4 kyr BP to today. In turn, this led to reduced stratification and eventual diminishment of hypoxia in the Bothnian sea (Jilbert et al., 2015). Modern circulation models indicate that the northward flowing deep-water in the Baltic Proper undergoes overturning just south of the Åland Sea and continue southward as surface currents (Elken

and Matthäus, 2008), thus restricting the inflow of saline waters to the Bothnian Sea. An important question is whether northward flowing current velocities were increased or diminished in response to shoaling of the Åland Sea?

The shallowing sills restricted but did not cut off the bottom water flow into the Bothnian Sea. Being connected to the North Sea via the Danish Strait, the Baltic Proper still had an inflow of saline deep-water traveling north. Our results indicate that this deep water strengthened the bottom currents in the survey area as indicated by the sub-bottom and bathymetric results as well as the grain size analysis (Figure 21). Modern water circulation modeling shows a northward flowing deep-water current with a velocity between 0-20 cm s<sup>-1</sup> at 100 m water depth (e.g. Meier, 2007; Westerlund et al., 2022).

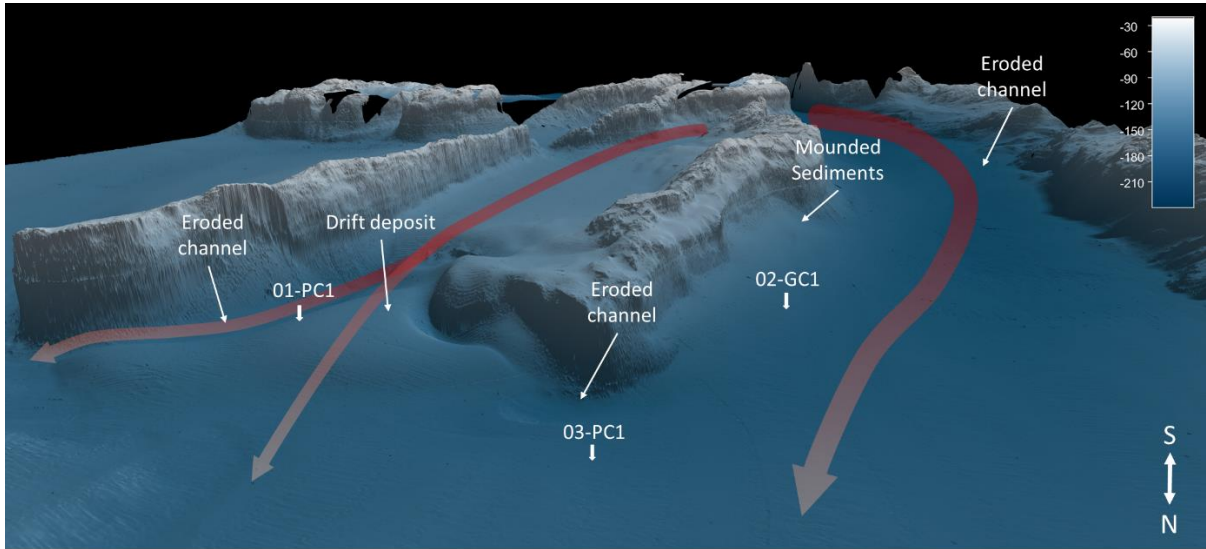


**Figure 21.** 3D-view of the bathymetry looking south of the survey area with a 3x depth exaggeration with core location and current created features marked out. Red graded arrows show the approximate bottom current direction with deep red representing a relative stronger current than the lighter red. Depth (m) scale in the top right corner. Shading with light source SW of the area.

5.3.1. Paleocurrent Strength Calculations Based on Shallowing from Isostatic Rebound  
 Paleobathymetric reconstructions indicate a shallowing of roughly 50 m in this area since 8 kyr BP due to isostatic rebound (Jilbert et al., 2015). To investigate how shallowing could affect current strength, a very simplified analytical model was developed. Assuming a constant volume flux in the surface ( $S_{VT}$ ) - and bottom ( $N_{VT}$ )- waters, shallowing reduces the cross-sectional area which would lead to increased current velocity ( $v$ ) (Equation 4).

$$v = \frac{N_{VT}}{H_B * W_D} \quad \text{Equation 4}$$

Where  $H_B$  is the thickness of the bottom current (modern measurements suggest that this thickness is ~50 m, Muchowski et al., in review) and  $W_D$  is the width of the deep-water passage, which is approximately 1000 m based on the bathymetric data. Decreasing  $H_B$  would lead to reduced cross-sectional area and thus a higher current velocity (Figure 22).

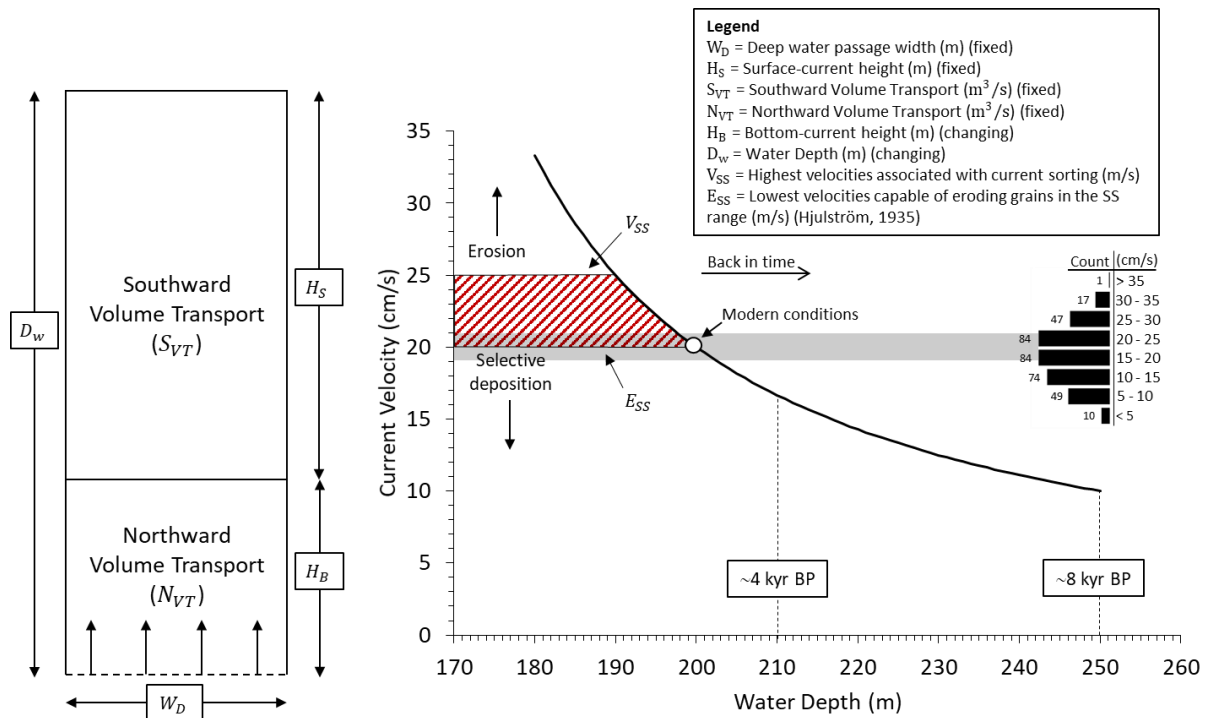


**Figure 22.** Conceptual model to the left illustrating a thinning bottom current and fixed surface current thickness. Right panel displays the result of the model which shows that shallowing results in higher current velocities. Histogram in the far right shows the mooring daily average during dec 2020 to dec 2021 (data from SMHI, 2021). Modern current conditions lie in the upper range of velocities associated with SS sorting and erosion of grains. Even a slight increase in water depth as seen e.g. 4 kyr BP reduces current velocities and thus decreases the chance of erosion and sorting by ~4 cm/s. Dates connected to water depth are interpreted from (Jilbert et al., 2015).

This suggests that if all parameters, but the cross-sectional area remains constant, the current velocity will increase as a result of shallowing. Importantly, it reveals the sensitivity of the current velocity on the depth of the trench, with relatively small changes being enough to lower the velocity so that it does not erode sediments. The conclusion is however limited by the simplicity of the model and very generalized assumptions. Several sources mention that the northward flow into the Åland Sea was strongly reduced with shallowing sills, as evidenced by, increased radiocarbon reservoir ages in the Gulf of Bothnia (Marmefelt and Omstedt, 1993; Raateoja, 2013). However, whether the shallowing and reduced deep-water flux is enough or too much to increase the general current velocity in the area is still not explored and is something future studies should elaborate on with more advanced oceanographic paleo-circulation models.

## 6. Conclusion

This study has presented geophysical and sedimentological data that shows how bottom currents influence and have been influenced by the marine geology in the Southern Quark. Bathymetric and sub-bottom data reveal numerous bedforms caused by current activity, such as eroded channels, drift deposits and truncated sub-bottom reflectors. Initial core descriptions from six marine sediment cores noted a coarse-grained sandy unit that capped 5 of the 6 cores. Grain size analysis from three of the six cores shows three distinct lithologic units with different SS properties, but all of which (except LU2 in 01-PC1) show a correlation indicating current sorting. The difference in SS properties between LU indicate some change in current activity. While the transition into sandy, erosional lag-type deposits (LU1) at the top of two cores indicates a relatively recent onset for strong current activity. Radiocarbon dating suggests the age of sediments in the drift deposit (whole core 01-PC1) are younger than those from LU1 in the two remaining cores. The onset of current activity is therefore suggested to be around 3 – 4 kyr BP during the transition from the Littorina to the Post Littorina Sea stage.

Modern bottom current measurements show a predominant northward current of ~20 cm/s which lies in the upper range of current strengths associated with current sorting. The results indicate that these high speeds only recently started to affect the area and the northward flowing current was weaker in the past. A simple model was created to explore the relationship between current strength and the with ~50 m shallowing of the sill that has resulted from isostatic rebound between 8 – 4 kyr BP. The model result showed that if the cross-sectional area is reduced, a shallower water passage, the current velocity increases. However, this involves a major assumption in that the volume flux remains constant through time.

Further research is needed to explore if the current velocity increased because of the shallowing in the Åland Sea since 8 kyr BP, or if it is the result of other processes currently not understood. Suggestions for future studies are to use more complete oceanographic paleo-circulation models to explore how other parameters may affect the currents in the Southern Quark during shallowing. Efforts to increase the resolution of sediment dating are also required to ad confidence to the assigned age of 3000-4000 <sup>14</sup>C years as defining the onset of the modern circulation system. Samples have been recovered and dried to perform complex isotopic dating of <sup>210</sup>Pb and <sup>137</sup>Cs to establish accurate the bulk sediment ages are. Further work could also explore compound specific <sup>14</sup>C dating of terrestrial and marine components.

## Acknowledgements

I would like to thank my supervisor Matt O'Regan for his incredible dedication and interest in this thesis that helped me so much during all phases of the project. A big thank you to my co-supervisors as well, Martin Jakobsson and Christian Stranne who guided me through the setup for the data processing as well as engaging in helpful discussions about oceanographic concepts in the Baltic Sea. I would for sure not have come close to the results I've now got if it wasn't for you three. I thank Carina Johansson who helped me in the beginning with the lab-work and with instructions for the equipment I used. I also thank Lisa Broder at ETH, Zürich for her help with the bulk carbon dating and TOC measurements.

Finally, I thank Zanna Zielfeldt for her unbelievable ability to cheer me up in times of stress and doubt. For all constructive comments and suggestions of change that made the final product better than what it was. This would not have been what is, if it wasn't for you, Thank You.

## References

- Ambjoern, C., Gidhagen, L., 1979. Water and material transports between the Gulf of Bothnia and the Baltic proper [current speed, current direction, water temperature, salinity, oxygen, total phosphorus, total nitrogen]. *Hydrology & Oceanography*, RHO 78.
- Andrén, E., Andrén, T., Kunzendorf, H., 2000. Holocene history of the Baltic Sea as a background for assessing records of human impact in the sediments of the Gotland Basin. *The Holocene* 10, 687–702. <https://doi.org/10.1191/09596830094944>
- Andrén, T., 2012. Baltic Sea Basin, Since the Latest Deglaciation, in: Bengtsson, L., Herschy, R.W., Fairbridge, R.W. (Eds.), *Encyclopedia of Lakes and Reservoirs*. Springer Netherlands, Dordrecht, pp. 95–102. [https://doi.org/10.1007/978-1-4020-4410-6\\_248](https://doi.org/10.1007/978-1-4020-4410-6_248)
- Andrén, T., Björck, S., Andrén, E., Conley, D., Zillén, L., Anjar, J., 2011. The Development of the Baltic Sea Basin During the Last 130 ka, in: Harff, J., Björck, S., Hoth, P. (Eds.), *The Baltic Sea Basin, Central and Eastern European Development Studies (CEEDES)*. Springer Berlin Heidelberg, Berlin, Heidelberg, pp. 75–97. [https://doi.org/10.1007/978-3-642-17220-5\\_4](https://doi.org/10.1007/978-3-642-17220-5_4)
- Andrén, T., Sohlenius, G., 1995. Late Quaternary development of the north-western Baltic Proper — Results from the clay-varve investigation. *Quaternary International* 27, 5–10. [https://doi.org/10.1016/1040-6182\(94\)00055-A](https://doi.org/10.1016/1040-6182(94)00055-A)
- Ben-Dor, E., Banin, A., 1989. Determination of organic matter content in arid-zone soils using a simple “loss-on-ignition” method. *Communications in Soil Science and Plant Analysis* 20, 1675–1695. <https://doi.org/10.1080/00103628909368175>

- Berglund, B.E., Sandgren, P., Barnekow, L., Hannon, G., Jiang, H., Skog, G., Yu, S.-Y., 2005. Early Holocene history of the Baltic Sea, as reflected in coastal sediments in Blekinge, southeastern Sweden. *Quaternary International* 130, 111–139.
- Björck, S., 1995. A review of the history of the Baltic Sea, 13.0–8.0 ka BP. *Quaternary International* 27, 19–40. [https://doi.org/10.1016/1040-6182\(94\)00057-C](https://doi.org/10.1016/1040-6182(94)00057-C)
- Björck, S., Andrén, T., Jensen, J., 2008. An attempt to resolve the partly conflicting data and ideas on the Ancyclus–Littorina transition. *Polish Geological Institute Special Papers* 23.
- Blott, S.J., Pye, K., 2001. GRADISTAT: a grain size distribution and statistics package for the analysis of unconsolidated sediments. *Earth Surface Processes and Landforms* 26, 1237–1248. <https://doi.org/10.1002/esp.261>
- Calder, B.R., Mayer, L.A., 2003. Automatic processing of high-rate, high-density multibeam echosounder data. *Geochemistry, Geophysics, Geosystems* 4. <https://doi.org/10.1029/2002GC000486>
- Culp, J., Strom, K., Parent, A., Romans, B., 2020. Advective sorting of silt by currents: a laboratory study. Preprint submitted to *Sedimentology*.
- Davies, J.L., 1964. A morphogenic approach to world shorelines. *Zeitschrift für Geomorphologie* 127–142. <https://doi.org/10.1127/zfg/mortensen/8/1964/127>
- Donner, J., Kankainen, T., Karhu, J.A., 1999. Radiocarbon ages and stable isotope composition of Holocene shells in Finland. *Quaternaria Series A*, 31–38.
- Dyer, K., 2001. Estuarine Circulation, in: Steele, J.H. (Ed.), *Encyclopedia of Ocean Sciences*. Academic Press, Oxford, pp. 846–852. <https://doi.org/10.1006/rwos.2001.0077>
- Ehlin, U., Ambjörn, C., Элин, У., Амбьёрн, С., 1977. Water Transport through the Åland Sea / Перемещение воды в Аландском море. *Ambio Special Report* 117–125.
- Elken, J., Matthäus, W., 2008. *Baltic Sea Oceanography*. H. Von Storch & A. Omstedt (Eds), *Assessment of Climate Change for the Baltic Sea Basin, Annex A.1.1. BALTEX Publication*, Springer 474.
- Folk, R.L., Ward, W.C., 1957. Brazos River Bar: A study in the significance of grain size parameters. *Journal of Sedimentary Research* 27, 3–26. <https://doi.org/10.1306/74D70646-2B21-11D7-8648000102C1865D>
- Fonseca, L., Mayer, L., 2007. Remote estimation of surficial seafloor properties through the application Angular Range Analysis to multibeam sonar data. *Marine Geophysical Researches* 28, 119–126. <https://doi.org/10.1007/s11001-007-9019-4>
- Glückert, G., 1995. The Baltic Ice Lake in south Finland and its outlets. *Quaternary International* 27, 47–51. [https://doi.org/10.1016/1040-6182\(94\)00059-E](https://doi.org/10.1016/1040-6182(94)00059-E)
- Gurvan, M., Bourdallé-Badie, R., Chanut, J., Clementi, E., Coward, A., Ethé, C., Iovino, D., Lea, D., Lévy, C., Lovato, T., Martin, N., Masson, S., Mocavero, S., Rousset, C., Storkey, D., Müeller, S., Nurser, G., Bell, M., Samson, G., Mathiot, P., Mele, F., Moulin, A., 2022. NEMO ocean engine 323. <https://doi.org/10.5281/zenodo.1464816>
- Gustafsson, B.G., Westman, P., 2002. On the causes for salinity variations in the Baltic Sea during the last 8500 years. *Paleoceanography* 17, 12-1-12–14. <https://doi.org/10.1029/2000PA000572>
- Håkanson, L., Bryhn, A., 2008. Introduction, Background and Aim, in: : : *Eutrophication in the Baltic Sea. Present Situation, Nutrient Transport Processes, Remedial Strategies*. Springer, pp. 1–21. [https://doi.org/10.1007/978-3-540-70909-1\\_1](https://doi.org/10.1007/978-3-540-70909-1_1)
- Hartz, N., 1912. Allerød-Gytje und Allerød-Mull. *Meddelelser fra Dansk Geologisk Forening* 4, 85–100.
- Heiri, O., Lotter, A., Lemcke, G., 2001. Loss on Ignition as a Method for Estimating Organic and Carbonate Content in Sediments: Reproducibility and Comparability of Results. *Journal of Paleolimnology* 25. <https://doi.org/10.1023/A:1008119611481>
- Hietala, R., Lundberg, P., Nilsson, J.A.U., 2007. A note on the deep-water inflow to the Bothnian Sea. *Journal of Marine Systems* 68, 255–264. <https://doi.org/10.1016/j.jmarsys.2006.12.004>
- Hjulström, F., 1935. *Studies of the morphological activity of rivers as illustrated by the River Fyris*. Almqvist & Wiksell, *Mesages from the institution of Geography at the University of Uppsala* 442–452.

- Holmlund, P., Jakobsson, M., Holmlund, E.S., O'Regan, M., Weidner, E., in press. Geophysical Surveys on sub marine land and rock lides and on alpine glaciers. will be published by the Swedish Radiation Safety Authority.
- Hsu, T.-J., 2016. Sediment Resuspension, in: Kennish, M.J. (Ed.), *Encyclopedia of Estuaries*. Springer Netherlands, Dordrecht, pp. 558–560. [https://doi.org/10.1007/978-94-017-8801-4\\_249](https://doi.org/10.1007/978-94-017-8801-4_249)
- Jakobsson, M., Björck, S., Alm, G., Andrén, T., Lindeberg, G., Svensson, N.-O., 2007. Reconstructing the Younger Dryas ice dammed lake in the Baltic Basin: Bathymetry, area and volume. *Global and Planetary Change* 57, 355–370. <https://doi.org/10.1016/j.gloplacha.2007.01.006>
- Jakobsson, M., Gyllencreutz, R., Mayer, L.A., Dowdeswell, J.A., Canals, M., Todd, B.J., Dowdeswell, E.K., Hogan, K.A., Larter, R.D., 2016. Mapping submarine glacial landforms using acoustic methods. *Geological Society, London, Memoirs* 46, 17–40. <https://doi.org/10.1144/M46.182>
- Jakobsson, M., Stranne, C., O'Regan, M., Greenwood, S.L., Gustafsson, B., Humborg, C., Weidner, E., 2019. Bathymetric properties of the Baltic Sea. *Ocean Science* 15, 905–924. <https://doi.org/10.5194/os-15-905-2019>
- Jensen, J.B., Bennike, O., Witkowski, A., Lemke, W., Kuijpers, A., 1999. Early Holocene history of the southwestern Baltic Sea: the Ancylus Lake stage. *Boreas* 28, 437–453. <https://doi.org/10.1111/j.1502-3885.1999.tb00233.x>
- Jilbert, T., Conley, D.J., Gustafsson, B.G., Funkey, C.P., Slomp, C.P., 2015. Glacio-isostatic control on hypoxia in a high-latitude shelf basin. *Geology* 43, 427–430. <https://doi.org/10.1130/G36454.1>
- Jilbert, T., Slomp, C.P., 2013. Rapid high-amplitude variability in Baltic Sea hypoxia during the Holocene. *Geology* 41, 1183–1186. <https://doi.org/10.1130/G34804.1>
- Kirk Cochran, J., 2014. Estuaries, in: *Reference Module in Earth Systems and Environmental Sciences*. Elsevier. <https://doi.org/10.1016/B978-0-12-409548-9.09151-X>
- Knudsen, M., 1900. Ein hydrographischer Lehrsatz. *Annalen der Hydrographie und Maritimen Meteorologie* 28, 316–320.
- Le Bas, T.P., Huvenne, V.A.I., 2009. Acquisition and processing of backscatter data for habitat mapping – Comparison of multibeam and sidescan systems. *Applied Acoustics, The Application of Underwater Acoustics for Seabed Habitat Mapping* 70, 1248–1257. <https://doi.org/10.1016/j.apacoust.2008.07.010>
- Lougheed, B.C., Filipsson, H.L., Snowball, I., 2013. Large spatial variations in coastal 14C reservoir age - a case study from the Baltic Sea. *Climate of the Past* 9, 1015–1028. <https://doi.org/10.5194/cp-9-1015-2013>
- Marmefelt, E., Omstedt, A., 1993. Deep water properties in the Gulf of Bothnia. *Continental Shelf Research* 13, 169–187. [https://doi.org/10.1016/0278-4343\(93\)90104-6](https://doi.org/10.1016/0278-4343(93)90104-6)
- McCave, I.N., Andrews, J.T., 2019. Distinguishing current effects in sediments delivered to the ocean by ice. I. Principles, methods and examples. *Quaternary Science Reviews* 212, 92–107. <https://doi.org/10.1016/j.quascirev.2019.03.031>
- McCave, I.N., Hall, I.R., 2006. Size sorting in marine muds: Processes, pitfalls, and prospects for paleoflow-speed proxies. *Geochemistry, Geophysics, Geosystems* 7. <https://doi.org/10.1029/2006GC001284>
- McCave, I.N., Manighetti, B., Robinson, S.G., 1995. Sortable silt and fine sediment size/composition slicing: Parameters for palaeocurrent speed and palaeoceanography. *Paleoceanography* 10, 593–610. <https://doi.org/10.1029/94PA03039>
- McCave, I.N., Thornalley, D.J.R., Hall, I.R., 2017. Relation of sortable silt grain-size to deep-sea current speeds: Calibration of the ‘Mud Current Meter.’ *Deep Sea Research Part I: Oceanographic Research Papers* 127, 1–12. <https://doi.org/10.1016/j.dsr.2017.07.003>
- Meier, H.E.M., 2007. Modeling the pathways and ages of inflowing salt- and freshwater in the Baltic Sea. *Estuarine, Coastal and Shelf Science, Timescale- and tracer-based methods for understanding the results of complex marine models* 74, 610–627. <https://doi.org/10.1016/j.ecss.2007.05.019>
- Mörner, N.-A., 1995. The Baltic Ice Lake-Yoldia Sea transition. *Quaternary International* 27, 95–98. [https://doi.org/10.1016/1040-6182\(94\)00065-D](https://doi.org/10.1016/1040-6182(94)00065-D)
- Moros, M., Kotilainen, A.T., Snowball, I., Neumann, T., Perner, K., Meier, H.E.M., Leipe, T., Zillén, L., Sinnighe Damsté, J.S., Schneider, R., 2020. Is ‘deep-water formation’ in the Baltic Sea a

- key to understanding seabed dynamics and ventilation changes over the past 7,000 years? *Quaternary International* 550, 55–65. <https://doi.org/10.1016/j.quaint.2020.03.031>
- Muchowski, J., Umlauf, L., Arneborg, L., Holtermann, P., Weidner, E., Humborg, C., Stranne, C., in review. Potential and Limitations of a Commercial Broadband Echosounder for Remote Observations of Turbulent Mixing. *Journal of Atmospheric and Oceanic Technology*.
- Palosuo, E., 1964. A Description of the Seasonal Variations of water Exchange Between the Baltic Proper and the Gulf of Bothnia. Publication of the Institute for Marine Research 1–32.
- Possnert, G., 2001. Reservoir ages in Baltic Sea sediment - A case study of an isolation sequence from the Litorina Sea stage. *Quaternary Science Reviews* 20, 1779–1785. [https://doi.org/10.1016/S0277-3791\(01\)00069-5](https://doi.org/10.1016/S0277-3791(01)00069-5)
- Pritchard, D., 1967. Observations of circulation in coastal plain estuaries. Washington DC Am Assoc Adv Sci, Lauf GH (ed) *Estuaries* 37–44.
- Raateoja, M., 2013. Deep-water oxygen conditions in the Bothnian Sea. *Boreal Environment Research* 18, 235–249. <https://helda.helsinki.fi/bitstream/handle/10138/229387/ber18-3-4-235.pdf?sequence=1>
- Reimer, P.J., Austin, W.E.N., Bard, E., Bayliss, A., Blackwell, P.G., Ramsey, C.B., Butzin, M., Cheng, H., Edwards, R.L., Friedrich, M., Grootes, P.M., Guilderson, T.P., Hajdas, I., Heaton, T.J., Hogg, A.G., Hughen, K.A., Kromer, B., Manning, S.W., Muscheler, R., Palmer, J.G., Pearson, C., Plicht, J. van der, Reimer, R.W., Richards, D.A., Scott, E.M., Southon, J.R., Turney, C.S.M., Wacker, L., Adolphi, F., Büntgen, U., Capano, M., Fahrni, S.M., Fogtmann-Schulz, A., Friedrich, R., Köhler, P., Kudsk, S., Miyake, F., Olsen, J., Reinig, F., Sakamoto, M., Sookdeo, A., Talamo, S., 2020. The IntCal20 Northern Hemisphere Radiocarbon Age Calibration Curve (0–55 cal kBP). *Radiocarbon* 62, 725–757. <https://doi.org/10.1017/RDC.2020.41>
- Sibson, R., 1981. A Brief Description of Natural Neighbor Interpolation. *Interpreting Multivariate Data*, John Wiley & Sons 21–36.
- SMHI, 2021. SMHI mooring station “Södra Kvarken”, financed by the Swedish Agency for Marine and Water Management.
- Sohlenius, G., Emeis, K.-C., Andrén, E., Andrén, T., Kohly, A., 2001. Development of anoxia during the Holocene fresh-brackish water transition in the Baltic Sea. *Marine Geology* 177, 221–242. [https://doi.org/10.1016/S0025-3227\(01\)00174-8](https://doi.org/10.1016/S0025-3227(01)00174-8)
- Sohlenius, G., Westman, P., 1998. Salinity and redox alternations in the northwestern Baltic proper during the late Holocene. *Boreas* 27, 101–114. <https://doi.org/10.1111/j.1502-3885.1998.tb00871.x>
- Swärd, H., O'Regan, M., Ampel, L., Ananiev, R., Chernykh, D., Flodén, T., Greenwood, S., Kylander, M., Mörth, C.-M., Preto, P., Jakobsson, M., 2015. Regional deglaciation and postglacial lake development as reflected in a 74 m sedimentary record from Lake Vättern, southern Sweden. *Gff -Uppsala- 00*, 1–19. <https://doi.org/10.1080/11035897.2015.1055510>
- Szymczycha, B., Zaborska, A., Bełdowski, J., Kuliński, K., Beszczyńska-Möller, A., Kędra, M., Pempkowiak, J., 2019. Chapter 4 - The Baltic Sea, in: Sheppard, C. (Ed.), *World Seas: An Environmental Evaluation (Second Edition)*. Academic Press, pp. 85–111. <https://doi.org/10.1016/B978-0-12-805068-2.00005-X>
- Udden, J.A., 1914. Mechanical composition of clastic sediments. *Geological Society of America Bulletin* 25, 655–744. <https://doi.org/10.1130/GSAB-25-655>
- Virtasalo, J.J., Hämäläinen, J., Kotilainen, A.T., 2014. Toward a standard stratigraphical classification practice for the Baltic Sea sediments: the CUAL approach. *Boreas* 43, n/a-n/a.
- Walker, M., Johnsen, S., Rasmussen, S.O., Popp, T., Steffensen, J.-P., Gibbard, P., Hoek, W., Lowe, J., Andrews, J., Björck, S., Cwynar, L.C., Hughen, K., Kershaw, P., Kromer, B., Litt, T., Lowe, D.J., Nakagawa, T., Newnham, R., Schwander, J., 2009. Formal definition and dating of the GSSP (Global Stratotype Section and Point) for the base of the Holocene using the Greenland NGRIP ice core, and selected auxiliary records. *Journal of Quaternary Science* 24, 3–17. <https://doi.org/10.1002/jqs.1227>
- Wastegård, S., Andrén, T., Sohlenius, G., Sandgren, P., 1995. Different phases of the Yoldia Sea in the north-western Baltic Proper. *Quaternary International* 27, 121–129. [https://doi.org/10.1016/1040-6182\(94\)00069-H](https://doi.org/10.1016/1040-6182(94)00069-H)

- Wentworth, C.K., 1922. A Scale of Grade and Class Terms for Clastic Sediments. *The Journal of Geology* 30, 377–392.
- Westerlund, A., Miettunen, E., Tuomi, L., Alenius, P., 2022. Refined estimates of water transport through the Åland Sea in the Baltic Sea. *Ocean Science* 18, 89–108. <https://doi.org/10.5194/os-18-89-2022>
- Widerlund, A., Andersson, P.S., 2011. Late Holocene freshening of the Baltic Sea derived from high-resolution strontium isotope analyses of mollusk shells. *Geology* 39, 187–190. <https://doi.org/10.1130/G31524.1>
- Winterhalter, B., 1992. Late-Quaternary stratigraphy of Baltic Sea basins - a review. *Bull Geol Soc Finland* 64, 189–194. <https://doi.org/10.17741/bgsf/64.2.007>
- Winterhalter, B., Flodén, T., Ignatius, H., Axberg, S., Niemistö, L., 1981. Chapter 1 Geology of the Baltic Sea, in: Voipio, A. (Ed.), Elsevier Oceanography Series, The Baltic Sea. Elsevier, pp. 1–121. [https://doi.org/10.1016/S0422-9894\(08\)70138-7](https://doi.org/10.1016/S0422-9894(08)70138-7)
- Zillén, L., Conley, D.J., Andrén, T., Andrén, E., Björck, S., 2008. Past occurrences of hypoxia in the Baltic Sea and the role of climate variability, environmental change and human impact. *Earth-Science Reviews* 91, 77–92. <https://doi.org/10.1016/j.earscirev.2008.10.001>

## Appendix A

*Table A.1. Raw data values for LOI and TOC. Dotted horizontal line indicates change of core.*

<b>Core</b>	<b>LU</b>	<b>Section</b>	<b>Depth (cm)</b>	<b>LOI %</b>	<b>TOC %</b>
EL17-IGV04-01-PC1	2	1	14	5.449574	2.46
EL17-IGV04-01-PC1	2	3	296	5.78653	2.94
EL17-IGV04-01-PC1	2	4	340	6.495454	4.04
EL17-IGV04-02-GC1	1	1	6	1.315658	0.66
EL17-IGV04-02-GC1	1	1	22	2.436703	1.33
EL17-IGV04-02-GC1	2	1	50	4.315979	2.12
EL17-IGV04-02-GC1	2	1	96	5.325692	3.18
EL17-IGV04-02-GC1	2	2	228	4.849925	3.67
EL17-IGV04-02-GC1	2	3	280	4.966036	1.92
EL17-IGV04-03-PC1	1	1	8	1.782122	0.86
EL17-IGV04-03-PC1	2	1	40	3.469888	1.93
EL17-IGV04-03-PC1	2	2	268	4.858624	2.89

## Appendix B

*Table B.1. Surface sortable silt results from all six recovered cores. Cores written in italic was further investigated.*

<b>Core</b>	<b>Depth (cm)</b>	<b>%&lt;63</b>	<b>%10-63</b>	<b>SS%</b>	<b>sumprod</b>	<b><math>\bar{SS}</math> (<math>\mu\text{m}</math>)</b>
01-PC	1-2	90.91164	27.51093	30.26117	84.43228	21.52134102
02-GC	1-2	24.3586	9.8828	40.57211	33.58075	29.90119191
03-PC	1-2	15.76677	7.14246	45.30071	24.45257	30.67813971
04-PC	1-2	35.39704	17.25387	48.74381	60.10281	32.57159161
05-GC	1-2	29.31138	12.03937	41.07406	40.55949	29.0466823
06-GC	1-2	42.84076	13.31019	31.06899	43.79463	26.8511448

**Table B.2.** Sortable silt results from core 01-PCI.

<b>ID</b>	<b>Depth (cm)</b>	<b>Section</b>	<b>LU</b>	<b>%&lt;63 μm (%)</b>	<b>%10-63 μm (%)</b>	<b>sumprod</b>	<b>SS%</b>	<b>SS̄ (μm)</b>
1PC-sec1-1cm	1	1	2	90.91163682	27.51092872	84.43227955	30.26117412	21.52134102
1PC-sec1-20cm	20	1	2	90.48685258	29.01266594	90.13972368	32.06285235	22.35185623
1PC-sec2-12.5cm	40	2	2	88.54271622	27.58380012	84.88119415	31.15309909	21.69781927
1PC-sec2-32.5cm	60	2	2	88.59499495	30.07140186	93.6279492	33.94255158	22.50013405
1PC-sec2-52.5cm	80	2	2	88.13084432	29.82199851	91.1846119	33.83832157	21.27705259
1PC-sec2-72.5cm	100	2	2	84.30045901	28.66062307	90.00208586	33.99818151	23.11009854
1PC-sec2-92.5cm	120	2	2	90.79616421	27.7266292	85.32421743	30.53722527	21.70056465
1PC-sec2-112.5cm	140	2	2	91.90531818	27.60906467	85.11387093	30.04076937	21.81992213
1PC-sec2-132.5cm	160	2	2	91.44473793	29.57925904	91.54753446	32.34659501	22.08703524
1PC-sec3-1.5cm	180	3	2	90.28155571	26.11477914	81.16727176	28.92592948	22.37842207
1PC-sec3-21.5cm	200	3	2	90.87402514	26.55271288	82.89810704	29.21925472	22.692177
1PC-sec3-41.5cm	220	3	2	89.24888711	26.58205992	84.06520756	29.78419203	23.62910105
1PC-sec3-61.5cm	240	3	2	90.27549163	28.81284995	90.21181549	31.91658049	22.89589731
1PC-sec3-81.5cm	260	3	2	90.25431102	29.38353834	91.60302795	32.55638208	22.58971691
1PC-sec3-101.5cm	280	3	2	90.04485166	25.92038348	80.56232702	28.78608049	22.37777963
1PC-sec3-121.5cm	300	3	2	89.67371829	25.55714293	79.5086751	28.50014856	22.44383095
1PC-sec3-141.5cm	320	3	2	89.85024983	27.04258591	85.24827545	30.09739646	23.39147029
1PC-sec4-11cm	340	4	2	88.86504018	23.20619085	72.2889456	26.11397103	22.53504336
1PC-sec4-31cm	360	4	2	88.52878837	21.70415241	68.21554265	24.51649097	23.172633
1PC-sec4-51cm	380	4	2	89.9625567	23.55110165	73.00631374	26.17878206	22.19597072
1PC-sec4-71cm	400	4	2	91.007307	24.15180931	74.6387668	26.53831885	21.9858845
1PC-sec4-91cm	420	4	2	92.03625495	21.95054709	66.93068386	23.84989166	21.09757046
1PC-sec4-111cm	440	4	2	90.63222498	22.50388604	69.3053366	24.82989472	21.75199064

**Table B.3.** Sortable silt results from core 02-GC1.

ID	Depth (cm)	Section	LU	%<63 $\mu\text{m}$ (%)	%10-63 $\mu\text{m}$ (%)	sumprod	SS%	$\overline{SS}$ ( $\mu\text{m}$ )
2GC-sec1-1cm	1	1	1	24.35860409	9.884773257	33.58540565	40.58021232	29.89499431
2GC-sec1-5cm	5	1	1	14.05413653	7.707542185	26.96336558	54.84180526	33.05950701
2GC-sec1-10cm	10	1	1	14.51601604	7.500773598	26.12824513	51.6723981	32.57049172
2GC-sec1-15cm	15	1	1	43.9450003	17.17875804	57.60187601	39.09149602	28.59086709
2GC-sec1-20cm	20	1	1	26.63241473	10.71830432	36.91738578	40.24533421	31.32231584
2GC-sec1-25cm	25	1	1	47.33455523	15.1542791	50.19323849	32.01525615	27.44405407
2GC-sec1-30cm	30	1	1	59.4923661	17.83865889	58.68893505	29.98478638	26.84248341
2GC-sec1-35cm	35	1	1	76.56327041	23.54146049	75.41102471	30.74772063	24.61431585
2GC-sec1-40cm	40	1	1	47.92993573	16.93757162	56.26953928	35.33818972	27.72051558
2GC-sec1-45cm	45	1	2	82.05966531	23.99329903	76.95738943	29.23884583	24.71606498
2GC-sec1-50cm	50	1	2	82.83865326	23.17634177	73.71478511	27.9776902	24.0613027
2GC-sec1-55cm	55	1	2	86.93938436	22.83588792	72.43306897	26.26644769	23.85267392
2GC-sec1-60cm	60	1	2	90.3582859	24.42703905	76.7245093	27.03353523	23.12620558
2GC-sec1-70cm	70	1	2	89.46242937	26.63698665	83.71385665	29.7744951	23.16789598
2GC-sec1-80cm	80	1	2	88.5697451	24.32685468	76.23146389	27.46632572	22.95725949
2GC-sec1-90cm	90	1	2	86.06577701	28.93577953	92.75383508	33.62054064	24.66799605
2GC-sec1-100cm	100	1	2	83.6968895	22.39950532	70.03065379	26.76264967	22.79263635
2GC-sec2-16cm	120	2	2	87.34166801	27.17840125	86.66176804	31.11733708	24.25508804
2GC-sec2-36cm	140	2	2	87.58107442	26.17147094	84.05304007	29.88256437	24.81947006
2GC-sec2-56cm	160	2	2	92.79362211	27.88297547	86.78996314	30.04837492	22.48055472
2GC-sec2-76cm	180	2	2	89.53727657	23.21809268	72.57627937	25.9312027	22.77925351
2GC-sec2-96cm	200	2	2	83.27371079	22.01736714	70.37473804	26.43975744	24.4426241
2GC-sec2-116cm	220	2	2	89.43094819	16.82613422	51.7360666	18.81466602	21.64435485
2GC-sec2-136cm	240	2	2	88.96649576	27.1275544	87.0356515	30.49187694	24.73911203
2GC-sec3-4.5cm	260	3	2	88.18765239	22.43296266	70.59386473	25.4377592	23.26339358
2GC-sec3-24.5cm	280	3	2	88.59260768	20.32859436	63.30624338	22.94615194	22.51423108
2GC-sec3-44.5cm	300	3	2	89.47603595	18.43806837	57.4273007	20.60671126	22.52453232
2GC-sec3-64.5cm	320	3	2	97.64532176	14.48191791	43.90043521	14.83114362	20.72615641
2GC-sec3-84.5cm	340	3	2	88.84487733	12.7025258	39.11044882	14.29742061	21.73558005
2GC-sec3-104.5cm	360	3	2	91.88014063	11.58469885	34.89622886	12.60849056	20.33348364
2GC-sec3-124.5cm	380	3	2	82.71022139	13.55392076	42.88857874	16.38723792	23.67200576
2GC-sec3-144.5cm	400	3	2	86.20285631	13.30284812	41.8651224	15.43202707	23.26801418

**Table B.4.** Sortable silt results from core 03-PCI.

ID	Depth (cm)	Section	LU	%<63 $\mu\text{m}$ (%)	%10-63 $\mu\text{m}$ (%)	sumprod	SS%	$\overline{\text{SS}}$ ( $\mu\text{m}$ )
3PC-sec1-1cm	1	1	1	15.76677139	7.143712796	24.45552719	45.30865969	30.67241503
3PC-sec1-5cm	5	1	1	16.43101129	8.055598495	28.04309861	49.02679668	32.49849191
3PC-sec1-10cm	10	1	1	35.527976	15.78169177	54.54936862	44.42046393	31.70571338
3PC-sec1-15cm	15	1	2	72.44374291	24.43654931	81.69439291	33.73175974	28.30739613
3PC-sec1-20cm	20	1	2	69.73838557	24.61772605	82.27238673	35.3001089	28.27555972
3PC-sec1-25cm	25	1	2	87.21816157	20.25376544	63.94311898	23.22195868	23.50228929
3PC-sec1-30cm	30	1	2	87.76421886	18.69610166	58.67261443	21.30264691	23.06294421
3PC-sec1-35cm	35	1	2	80.73735956	19.40135204	62.25777984	24.03020379	24.75284098
3PC-sec1-40cm	40	1	2	79.28106495	22.18840964	72.85408435	27.9870227	26.66707748
3PC-sec1-60cm	60	1	2	86.79325407	17.62928062	55.18215322	20.31180973	22.87722984
3PC-sec1-80cm	80	1	2	91.82952989	15.39658353	47.27878807	16.7664841	21.55768598
3PC-sec1-100cm	100	1	2	88.84034251	25.57242804	81.93585977	28.78470222	24.63259095
3PC-sec1-120cm	120	1	2	97.30763907	17.08915592	51.88461671	17.56198803	20.82415234
3PC-sec2-10.5cm	140	2	2	97.00513119	14.00138181	42.76926476	14.43365072	21.21367427
3PC-sec2-30.5cm	160	2	2	95.09648832	14.20221747	43.76916776	14.93453409	21.79879071
3PC-sec2-50.5cm	180	2	2	96.60654252	12.44753805	38.30998909	12.8847775	21.70876651
3PC-sec2-70.5cm	200	2	2	84.86797854	13.45433622	42.72399528	15.85325401	23.93834258
3PC-sec2-90.5cm	220	2	2	82.94073512	11.66724776	36.86074637	14.06696931	23.55493108
3PC-sec2-110.5cm	240	2	2	85.24322926	14.37526801	45.550346	16.86382383	23.77561902
3PC-sec2-130.5cm	260	2	2	89.46060455	12.48009377	39.2045335	13.95037943	23.13543208
3PC-sec2-150.5cm	280	2	2	87.00320465	14.32911523	45.06892203	16.46964073	23.22592259
3PC-sec3-18cm	300	3	3	100	5.214781403	13.23865523	5.214781403	12.66293024
3PC-sec3-38cm	320	3	3	98.58514559	7.882323894	20.9577201	7.99544784	14.27950132
3PC-sec3-58cm	340	3	3	96.80805783	7.522685738	20.17265833	7.770722713	14.60810685
3PC-sec3-78cm	360	3	3	100	9.817439756	26.31005238	9.817439756	14.58407394
3PC-sec3-98cm	380	3	3	100	10.77328006	28.87167347	10.77328006	14.58412253
3PC-sec3-118cm	400	3	3	97.61637992	20.53105597	56.17648057	21.0323882	15.42779928
3PC-sec3-138cm	420	3	3	99.91484994	20.29647005	55.53120454	20.31376723	15.42520838